ADVANCED FUNCTIONAL MATERIALS
www.afm-journal.de

Multifunctional BPs/MT@PLGA-ALE Nanospheres for Treatment of Osteoporotic Fracture with Near-Infrared Irradiation

Kai Zheng, Jiaxiang Bai, Wanling Chen, Yaozeng Xu, Huilin Yang, Wei Li, Penghui Li, Liping Tong,* Huaiyu Wang,* Paul K. Chu, and Dechun Geng**

Osteoporotic fracture, which is a clinical complication of osteoporosis featured with the imbalance of bone homeostasis. Non-surgical intervention is frequently required post-operatively to ameliorate the fracture healing. Nevertheless, current non-surgical therapies are mostly performed in a non-targeted manner without giving enough consideration to the pathological characteristics of osteoporosis. Therefore, it is highly desirable to develop an optimal strategy for promoting fracture healing under osteoporotic conditions. In this study, a multifunctional therapeutic nanoplatform is designed to work in conjunction with near-infrared irradiation. Specifically, poly (lactic-co-glycolic acid) (PLGA) is functionalized with alendronate (ALE) and black phosphorus nanosheets (BPs) together with melatonin (MT) molecules are encapsulated by PLGA-ALE to produce the multifunctional BPs/MT@PLGA-ALE nanospheres. In this structure, BPs degrade gradually and deliver mild photothermal effects to facilitate bone regeneration, whereas MT has the dual-capability of suppressing osteoclastogenesis and promoting osteogenesis. Moreover, ALE endows the nanoplatform with the reliable bone-targeting capacity to improve the therapeutic effects. The combination of BPs/MT@PLGA-ALE nanospheres and photothermal therapy significantly improve post-surgical healing of osteoporotic fracture by modulating the tumor necrosis factor and cell death-related signaling pathways. This study reveals a promising strategy to treat osteoporotic fracture and broadens the application of nanomaterials in the biomedical field.

1. Introduction

Osteoporotic fracture is one of the serious clinical consequences of osteoporosis characterized by reduced bone mineral density and quality, bone micro-structural damage, and mechanical strength deterioration.[1] The occurrence of osteoporotic fracture is especially high for older people giving rise to high recurrence and disablement rates.[2] It is estimated that as many as one-third of female and one-fifth of male people over 50 years old have osteoporotic fractures during their remaining lifetime.[3] Statistically, osteoporosis contributes to fragility fracture every 3 s worldwide,[4] leading to a substantial burden on the health cost. Generally, surgery is the first choice for bone fracture but surgical intervention alone fails to prevent further aggravation and pathological alteration of osteoporosis. Therefore, in addition to surgical operations, non-surgical, and systemic treatments for the prevention of recurrent fracture and maintenance of long-term post-operative efficacy are necessary.[5] However, most of the current systemic therapies for osteoporosis are performed in a non-targeted

K. Zheng, J. Bai, Y. Xu, H. Yang, D. Geng
Department of Orthopedics
The First Affiliated Hospital of Soochow University
188 Shizi Road, Suzhou, Jiangsu 215006, China
E-mail: szgengdc@suda.edu.cn

W. Chen, W. Li, P. Li, L. Tong, H. Wang
Center for Human Tissues and Organs Degeneration
Shenzhen Institute of Advanced Technology
Chinese Academy of Sciences
Shenzhen 518055, China
E-mail: ph.li@siat.ac.cn; lp.tong@siat.ac.cn; hy.wang1@siat.ac.cn

P. K. Chu
Department of Physics
Department of Materials Science and Engineering, and Department of Biomedical Engineering
City University of Hong Kong
Tat Chee Avenue, Hong Kong 999077, China

The ORCID identification number(s) for the author(s) of this article can be found under https://doi.org/10.1002/adfm.202214126.

DOI: 10.1002/adfm.202214126

manner without considering the pathological characteristics of such disorders.

Communication and coupling between osteoblasts and osteoclasts are indispensable during the process of bone remodeling.[6] When osteoblasts form new bones, osteoclasts play the role of bone resorption resulting in a delicate balance. However, osteoporotic patients show excessive bone resorption and insufficient bone formation as the typical dyshomeostasis of bone metabolism.[7] When bone fractures occur under such conditions, disorder of the microenvironment delays healing or leads to even nonunion of the fractures after surgery. Hence, treatment of bone fractures must take restoration of bone homeostasis into account but so far, antiresorptive drugs and anabolic drugs which are still the first-line drugs for osteoporosis only inhibit bone resorption or promote bone formation unilaterally. Moreover, these medications cannot effectively target the sites of lesion after intravenous or subcutaneous administration, consequently compromising the therapeutic effects and causing adverse effects. For instance, long-term usage of antiresorptive drugs may increase the potential risk of breast cancer, cardiovascular disease, venous thromboembolism, atypical fractures, and osteonecrosis of the jaw.[8] Furthermore, overuse of anabolic drugs increases the incidence of osteosarcoma[9] and hence, it is necessary to develop innovative therapies with higher efficacy and fewer adverse effects to ameliorate bone healing after surgical treatment of osteoporotic fractures.

Photothermal nanomaterials that respond to near-infrared (NIR) irradiation have garnered much attention as they can convert NIR light into heat in vivo and corresponding photothermal therapy (PTT) is minimally invasive, rapid, and spatiotemporally controllable.[10] Notably, the temperature of PTT can be very fastidious owing to excessive heat can induce thermal resistance and cell death.[11] NIR-mediated PTT not only ablates tumors by generating hyperthermia (>50 °C),[12] but also delivers pro-osteogenic effects within a proper range of temperature (40–42 °C).[13] Therefore, PTT holds large potential but still needs further improvement to meet the multi-functional requirements of targeted delivery, osteogenesis promotion, as well as osteoclastogenesis inhibition.

Herein, multifunctional nanospheres (NSs) are described for the post-operative therapy of osteoporotic fractures. Black phosphorus nanosheets (BPs) are the photothermal agents because they not only provide excellent NIR-mediated photothermal effects, but also degrade gradually into PO_4^{3-} in the physiological environment to facilitate bone regeneration by contributing to the formation of hydroxyapatite (HA, the main inorganic component in natural bone).[14] Melatonin (MT), a type of indole neuroendocrine hormone secreted by the pineal gland for improving bone health through its dual actions on osteoclasts and osteoblasts,[15] can inhibit periprosthetic osteolysis by suppressing osteoclastogenesis via the NF-κB signaling pathway and simultaneously promoting osteogenesis via the Wnt/β-catenin signaling pathway.[16] Poly(lactide-co-glycolide) (PLGA, a biodegradable and biocompatible polymer approved by FDA)[17] is utilized as the basic material to encapsulate BPs and MT in the structure and the polymer chain of PLGA is functionalized with alendronate (ALE, a kind of bisphosphonate that can accumulate at the active sites of bone resorption)[18] to enable bone targeting. The multifunctional BPs/MT@PLGA-ALE NSs fabricated by oil-in-water emulsion solvent evaporation target the fractured bone tissues due to the high bone-affinity of ALE and work in conjunction with NIR irradiation to restore the metabolic equilibrium between bone formation and bone resorption (**Scheme 1**).

2. Results and Discussion

2.1. Sample Fabrication and Characterization

Fabrication of the BPs/MT@PLGA-ALE NSs proceeds with the preparation of BPs and functionalization of PLGA. The BPs are prepared by a modified liquid exfoliation method reported by our group previously,[19] and the PLGA polymer used to prepare the NSs is bound terminally to the bone targeting ligand ALE by amidation between the EDC/NHS activated PLGA and acetic acid modified ALE (Figure S1a, Supporting Information). The chemical structure of PLGA-ALE is determined by ^{1}H nuclear magnetic resonance spectroscopy (^{1}H NMR) and Fourier transform infrared spectroscopy (FTIR). As shown in Figure S1b,c (Supporting Information), the additional chemical shifts of ALE at 2.99 and 1.96 ppm are observed from the ^{1}H NMR spectrum and a new band at 1019 cm^{-1} appears from the FTIR spectrum to confirm the successful fabrication of PLGA-ALE.[20]

The BPs/MT@PLGA-ALE NSs are fabricated by the oil/water emulsion solvent evaporation method.[21] The photothermal agent BPs and MT drug for restoration of bone homeostasis are encapsulated into the PLGA-ALE NSs as illustrated in **Figure 1**a. Briefly, the BPs, PLGA-ALE, and MT are introduced into dichloromethane (DCM) and sonicated to form a homogeneous dispersion as the oil phase. It is mixed with an aqueous solution of polyvinyl alcohol (PVA) to form the oil/water emulsion and after stirring and evaporation of DCM, the dispersion of BPs/MT@PLGA-ALE NSs is obtained. By using a similar strategy, BPs/MT@PLGA-ALE NSs and the counterparts including PLGA-ALE NSs, MT@PLGA-ALE NSs, and BPs@PLGA-ALE NSs are prepared. The scanning electron microscopy (SEM) images in Figure 1b,e confirms high-yield fabrication of the NSs and reveal the similar uniform spherical morphology with a smooth surface. The average hydrodynamic size of the NSs is 165–185 nm and the zeta potentials vary from −13.4 to −20.17 mV (Figure S2, Supporting Information). As shown in Figure 1f, the MT band at 1217 cm^{-1} in the FTIR spectra of MT@PLGA-ALE NSs and BPs/MT@PLGA-ALE NSs discloses encapsulation of MT. The Raman scattering spectra of BPs, BPs@PLGA-ALE NSs and BPs/MT@PLGA-ALE NSs (Figure 1g) exhibit three prominent Raman peaks at 359.7, 436.2, and 463.5 cm^{-1} assigned to one out-of-plane phonon mode (A^1_g) and two in-plane modes (B^2_g and A^2_g) of BPs, respectively. The transmission electron microscopy (TEM) images in Figure S3a,b (Supporting Information) confirms the spherical structures of PLGA-ALE NSs and BPs/MT@PLGA-ALE NSs, which can also be seen from BPs/MT@PLGA-ALE NSs that BPs are incorporated inside each NS with PLGA-ALE shell. Energy dispersive X-ray spectroscopy (EDS) shows a uniform distribution of phosphorous in BPs@PLGA-ALE NSs and BPs/MT@PLGA-ALE NSs with concentrations of 5.8% and 5.19%, respectively (Figure S3, Supporting Information). These results corroborate

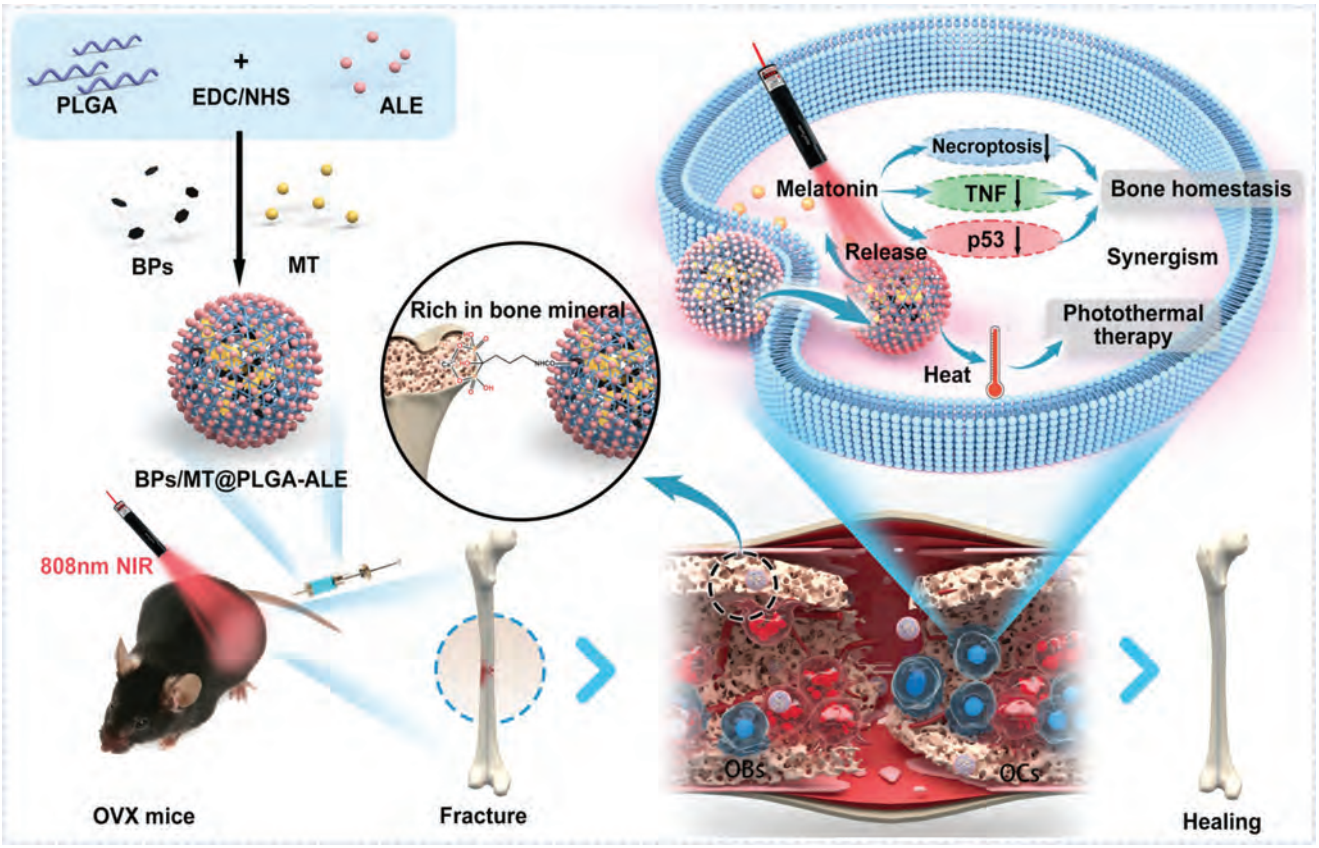

Scheme 1. Schematic illustration of the multifunctional BPs/MT@PLGA-ALE NSs for the treatment of osteoporotic fracture with NIR irradiation. ALE: alendronate; BPs: black phosphorus nanosheets; MT: melatonin; OBs: osteoblasts; OCs: osteoclasts; OVX: ovariectomy.

successful introduction of BPs into the BPs@PLGA-ALE NSs and BPs/MT@PLGA-ALE NSs. According to inductively-coupled plasma atomic emission spectrometry (ICP-AES) and UV–vis–NIR spectrophotometry, the loaded contents of BPs and MT in BPs/MT@PLGA-ALE NSs are 5.91 ± 0.17% and 2.73 ± 0.15%, respectively (Table S1, Supporting Information).

The UV–vis–NIR absorption spectra are presented in Figure 1h. In comparison with PLGA-ALE NSs and MT@PLGA-ALE NSs, pronounced absorption in the NIR region is observed from the BPs@PLGA-ALE NSs and BPs/MT@PLGA-ALE NSs due to the innate absorption characteristics of BPs. The photothermal characteristics are examined under NIR laser irradiation (808 nm, 1.5 W cm^{-2}). As shown in Figure 1i, a remarkable temperature rise of ≈26 °C is observed from the BPs@PLGA-ALE NSs and BPs/MT@PLGA-ALE NSs within 15 min of NIR irradiation and the temperature increase of BPs is 20 °C under the same NIR irradiation. In contrast, negligible temperature changes are observed from the PLGA-ALE NSs and MT@PLGA-ALE NSs. The stability of BPs before and after encapsulation is studied by storing the aqueous solutions of BPs and BPs/MT@PLGA-ALE NSs with the same amount of BPs at room temperature for 7 days. As shown in Figure S4a (Supporting Information), the color of the BPs solution becomes lighter after two days but that of the BPs/MT@PLGA-ALE NSs does not change. The absorption intensity of the BPs solution decreases with time and the absorbance of the BPs/MT@PLGA-ALE NSs solution is more stable (Figure S4b,c, Supporting Information). The BPs/MT@PLGA-ALE NSs solution shows better photothermal characteristics than the BPs solution after storage for 7 days (Figures S4d,e, Supporting Information), verifying that encapsulation of BPs inside the PLGA-ALE shells retards oxidation of BPs to improve the stability. The degradation behavior is investigated in PBS to simulate the physiological conditions at 37 °C. BPs agitated in PBS degrade faster than those dispersed in water at room temperature, as shown by more color fading and photothermal loss within 24 h (Figure S5, Supporting Information). In contrast, the properties of BPs/MT@PLGA-ALE NSs in PBS at 37 °C decline more slowly (Figure S5, Supporting Information) and the results disclose the BPs after encapsulation have better stability.

2.2. In Vitro Biocompatibility

Biocompatibility is a prerequisite to biomedical application of nanomaterials and the possible cytotoxicity of various NSs is investigated. The MC3T3-E1 and RAW264.7 cells are incubated separately with different concentrations of PLGA-ALE NSs, MT@PLGA-ALE NSs, BPs@PLGA-ALE NSs, and BPs/MT@PLGA-ALE NSs for 24 and 72 h and the viability is determined by the cell counting kit-8 (CCK-8) assay. As shown in **Figure 2**a, the viability of the two types of cells decreases with increasing nanosphere concentrations and culturing time, especially the ones incubated with the BPs@PLGA-ALE NSs and

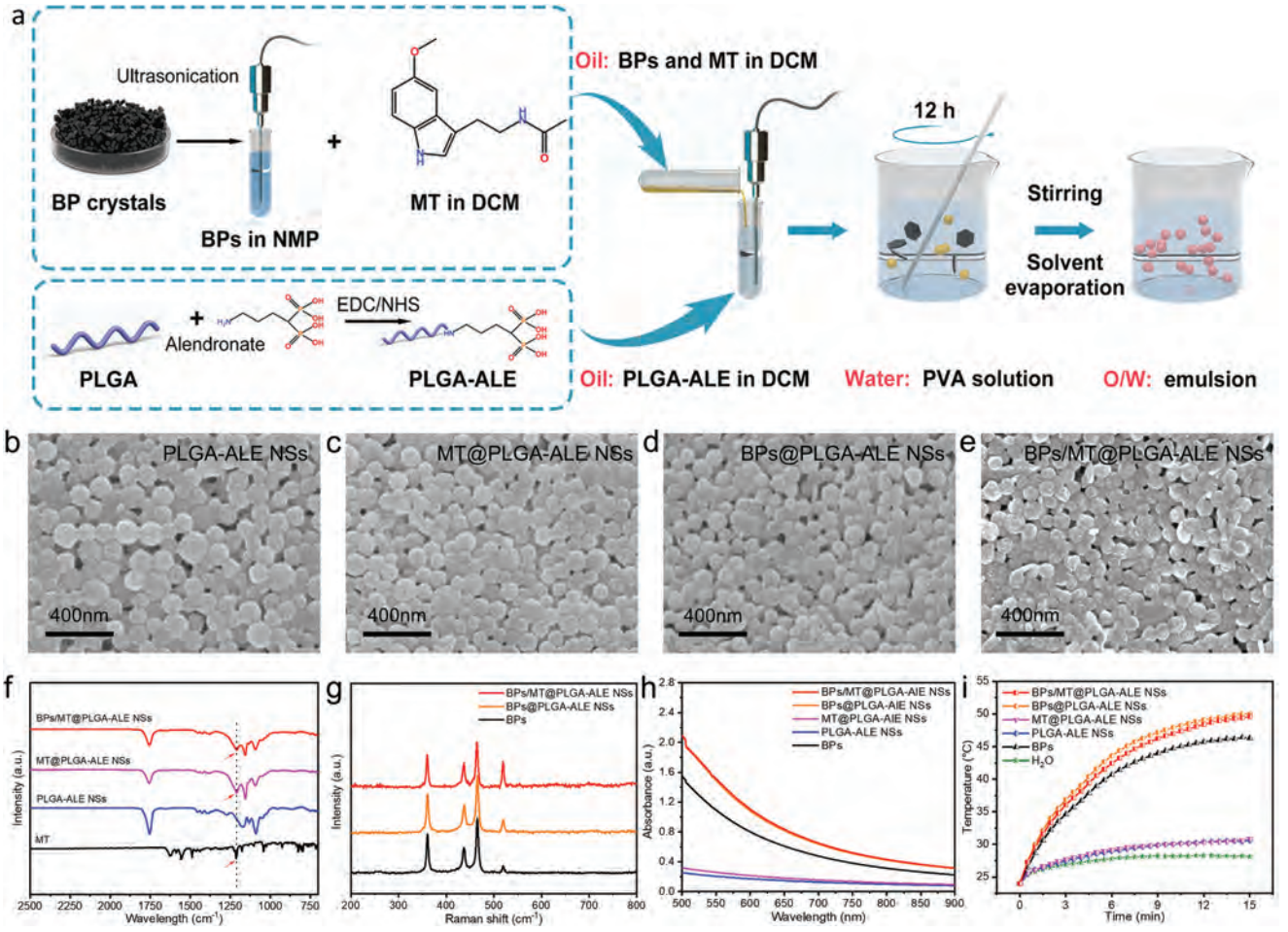

Figure 1. Fabrication and characterization of the BPs/MT/PLGA-ALE NSs. a) Schematic illustration of the fabrication of the BPs/MT/PLGA-ALE NSs; b–e) SEM images of the PLGA-ALE NSs, MT@PLGA-ALE NSs, BPs@PLGA-ALE NSs, and BPs/MT@PLGA-ALE NSs; f) FTIR spectra of the MT, PLGA-ALE NSs, MT@PLGA-ALE NSs, and BPs/MT@PLGA-ALE NSs; g) Raman scattering spectra acquired from the BPs, BPs@PLGA-ALE NSs and BPs/MT@PLGA-ALE NSs; h,i) Absorption spectra and photothermal heating curves of the BPs, PLGA-ALE NSs, MT@PLGA-ALE NSs, BPs@PLGA-ALE NSs, and BPs/MT@PLGA-ALE NSs.

BPs/MT@PLGA-ALE NSs. However, no significant cytotoxicity is detected from these two kinds of nanospheres at concentrations below 12.5 μg mL^{-1} (marked by red rectangles). Hence, the concentration of various NSs is chosen to be 12.5 μg mL^{-1} in subsequent in vitro studies. The RAW264.7 and MC3T3-E1 cells incubated with different NSs are examined by live/dead fluorescent staining which further confirms good cytocompatibility at a concentration of 12.5 μg mL^{-1} as manifested by negligible dead cells after 72 h (Figure 2b,c). The mild to moderate photothermal effects of the NSs on mammalian cells are assessed by controlling the temperature below 45 °C during 808 nm NIR laser irradiation. As shown in Figure S6 (Supporting Information), no significant increase in dead cells is observed from all the groups compared to the experimental groups without NIR irradiation to confirm the biological safety and mild hyperpyrexia.[22] The potential risk of organ damage arising from the NSs is evaluated and after weekly intravenous administration of different NSs for 3 months, the mice are sacrificed and the major organs including heart, liver, spleen, lung, and kidney are collected for hematoxylin-eosin (H&E) staining and histological analysis. No histopathological changes can be found from the major organs of the different groups (Figure S7, Supporting Information) indicative of the good in vivo biosafety.

2.3. In Vitro Osteoclastogenesis

The effects of the NSs and NIR irradiation on osteoclastogenesis are investigated in vitro. The RAW264.7 cells are induced by RANKL to form osteoclasts and then treated with different NSs with or without NIR irradiation. After different treatments, F-actin ring formation of osteoclasts is assessed by phalloidin staining to evaluate the functions of osteoclasts.[23] As shown in Figure S8 (Supporting Information), there is no evident difference in the average areas of F-actin ring formation when the osteoclasts are incubated with PLGA-ALE NSs and MT@PLGA-ALE NSs with or without NIR irradiation, whereas the average F-actin areas of osteoclasts in the two BPs-containing groups (BPs@PLGA-ALE and BPs/MT@PLGA-ALE NSs) decrease significantly after NIR irradiation. Similarly, the TRAP-positive

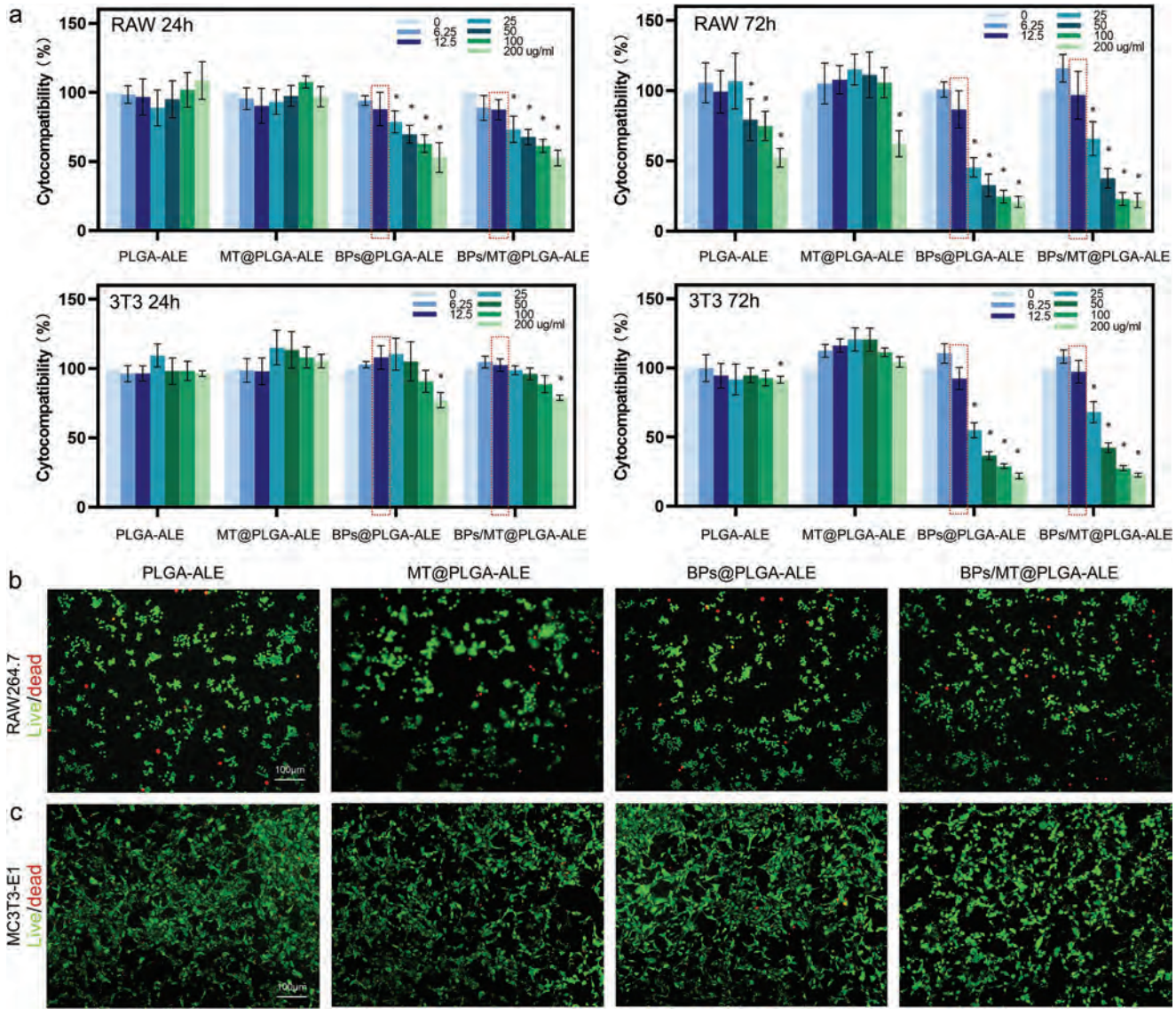

Figure 2. Cytocompatibility of the PLGA-ALE NSs, MT@PLGA-ALE NSs, BPs@PLGA-ALE NSs, and BPs/MT@PLGA-ALE NSs. a) Viability of the RAW264.7 and MC3T3-E1 cells after incubation with various NSs at different concentrations (0–200 μg mL^{-1}) for 24 and 72 h ($n = 6$ per group, * denotes $p < 0.05$ compared to the basal group); b,c) Live/dead staining of the RAW264.7 and MC3T3-E1 cells after incubation with various NSs at a concentration of 12.5 μg mL^{-1} for 72 h.

multinucleated osteoclasts of the two BPs-containing groups are inhibited after NIR irradiation (Figure S9, Supporting Information). These results indicate negligible effects on osteoclast differentiation with NIR irradiation alone and osteoclastogenesis suppression partly originates from NIR-induced heating of BPs. Therefore, both the BPs-containing groups undergo NIR irradiation in the following experiments.

To further investigate the effects of BPs/MT@PLGA-ALE NSs on osteoclastogenesis, the expression of key osteoclastogenesis-related genes including matrix metallopeptidase 9 (MMP9), nuclear factor of activated T-cells, cytoplasmic, calcineurin-dependent 1 (NFATc1), Tartrate-resistant acid phosphatase (TRAP), and ATPase H^+ Transporting V0 Subunit D2 (Atp6v0d2) are analyzed for the different groups. As shown in **Figure 3**a, the osteoclastogenesis-related gene levels of cells incubated with the PLGA-ALE NSs are significantly up-regulated after RANKL stimulation (Group II vs. Group I). However, compared to the RANKL-simulated PLGA-ALE group (Group II), the expressions of these genes are more or less down-regulated in the RANKL-simulated cells treated by MT@PLGA-ALE, BPs@PLGA-ALE+NIR, and BPs/MT@PLGA-ALE+NIR (Group III–V), and the BPs/MT@PLGA-ALE+NIR group (Group V) exhibits the best effects in suppressing osteoclastogenesis. Western blot analysis further verifies that the protein levels of osteoclastic markers including MMP9, NFATc1, and TRAP, and c-fos of the RANKL-simulated cells can be down-regulated in the modified groups (Group III–V), especially after the BPs/MT@PLGA-ALE+NIR treatment (Figure S10, Supporting Information). Moreover, compared to PLGA-ALE NSs, MT@PLGA-ALE NSs

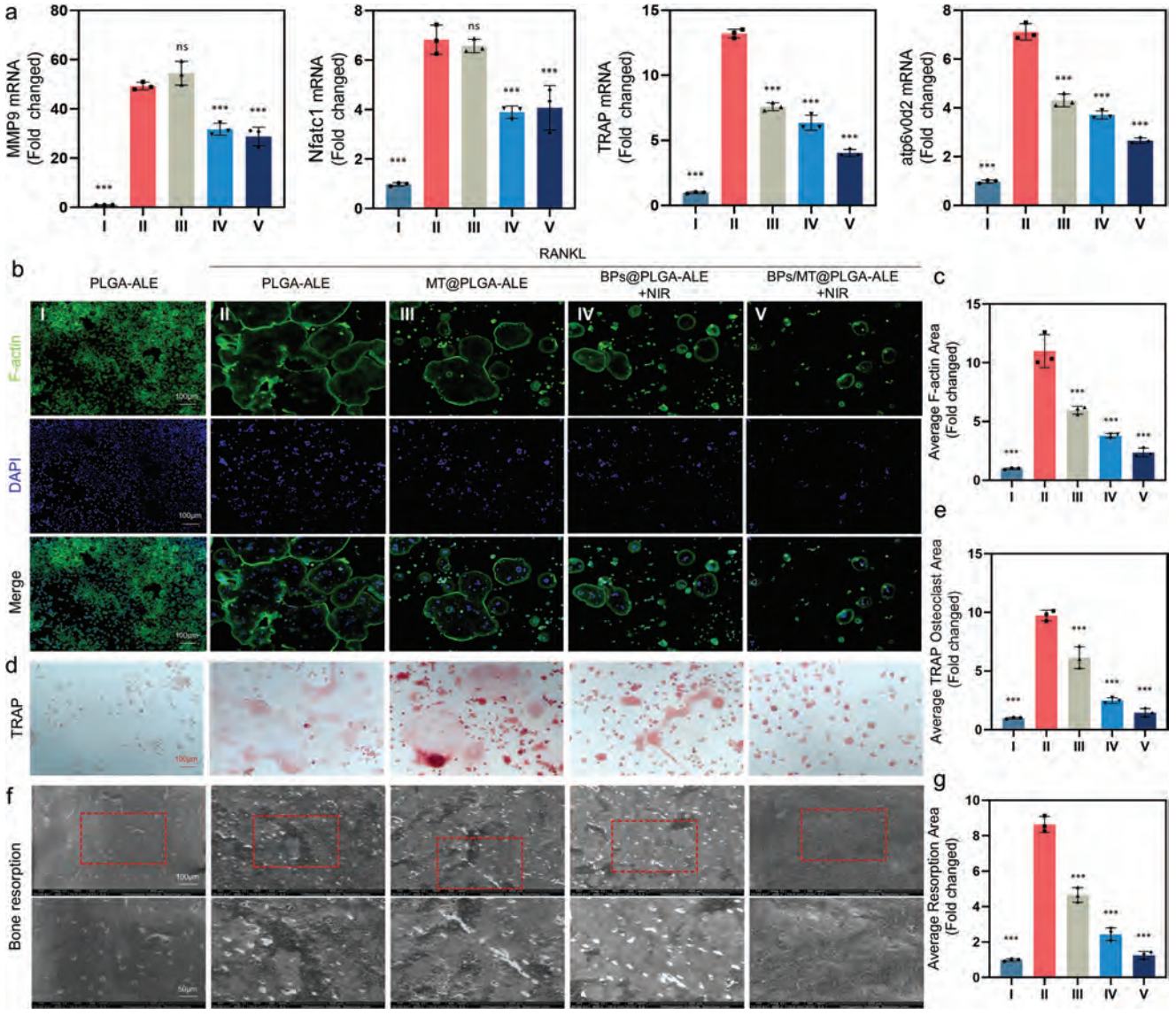

Figure 3. In vitro osteoclastogenesis of the RAW264.7 cells after different treatments (I: PLGA-ALE, II: PLGA-ALE + RANKL induction, III: MT@PLGA-ALE + RANKL induction, IV: BPs@PLGA-ALE+NIR + RANKL induction, V: BPs/MT@PLGA-ALE+NIR + RANKL induction). a) Gene levels of MMP9, Nfatc1, TRAP, and atp6v0d2; b) Fluorescent staining of F-actin (green); c) Quantitative evaluation of the F-actin areas; d) TRAP staining; e) Quantitative evaluation of the TRAP-positive areas; f) Bone resorption pits; g) Quantitative evaluation of the bone resorption areas ($n = 3$ per group, *** denotes $p < 0.001$ compared to the PLGA-ALE + RANKL group).

suppress the F-actin ring formation and TRAP activity of osteoclasts to a certain extent, and the BPs@PLGA-ALE NSs and BPs/MT@PLGA-ALE NSs with NIR irradiation show better inhibitory effects (Figure 3b–e). As mature osteoclasts are multinucleated giant cells with the bone resorption capacity, an osteoclastic pit formation assay is performed to further determine the effects of various treatments on bone resorption.[24] As shown in Figure 3f,g, obvious reduction in the bone resorption areas can be observed from the samples in the modified groups (Group III–V), particularly the BPs/MT@PLGA-ALE+NIR group (Group V). All in all, the BPs/MT@PLGA-ALE+NIR group shows the best effects in suppressing osteoclastogenesis in vitro, which can be ascribed to the combined effects of ALE, MT and BPs-based photothermal treatment.

2.4. In Vitro Osteogenesis

In addition to the suppression of osteoclastogenesis, fracture healing is associated with increased osteoblast differentiation and osteogenesis thereafter.[25] The alkaline phosphatase (ALP) activity (a typical marker for the early stage of osteoblast differentiation)[26] of MC3T3-E1 cells is evaluated after the treatment with different NSs with or without 808 nm NIR irradiation. As shown in Figure S11 (Supporting Information), the PLGA-ALE and MT@PLGA-ALE groups show almost the same ALP activity before and after NIR irradiation, but significant increases are observed from the BPs@PLGA-ALE and BPs/MT@PLGA-ALE groups upon NIR irradiation. The results indicate that NIR irradiation alone can hardly induce differentiation of osteoblasts,

whereas the photothermal effects of BPs rendered by NIR irradiation contributes to enhanced osteogenesis. Therefore, the effects of the BPs@PLGA-ALE NSs and BPs/MT@PLGA-ALE NSs on osteogenesis are evaluated under NIR irradiation.

The MC3T3-E1 cells in different groups are subjected to osteogenic induction for 3 days and the expression of key osteogenesis-related genes including collagen type I alpha 1 (COL1A1), ALP, runt-related transcription factor 2 (Runx2) and osteocalcin (OCN) are investigated. As shown in **Figure 4**a, the levels of these genes are significantly up-regulated after osteogenic induction (Group II vs. Group I) and can be further enhanced after treatment with MT@PLGA-ALE, BPs@PLGA-ALE+NIR, and BPs/MT@PLGA-ALE+NIR (Group III–V). In particular, the BPs/MT@PLGA-ALE+NIR group exhbits the best pro-osteogenic effects. Western blot analysis further verifies that in vitro osteogenesis after osteogenic induction follows the order of BPs/MT@PLGA-ALE+NIR > BPs@PLGA-ALE+NIR > MT@PLGA-ALE > PLGA-ALE (Figure S12, Supporting Information). In addition, the cells in the modified groups (Group III–V) show enhanced ALP activity, especially in the BPs/MT@PLGA-ALE+NIR group (Figure 4b,c). After osteogenic induction for 21 days, alizarin red S staining is performed to access mineralization. As shown in Figure 4d, relatively few and small mineralized nodules are detected from the PLGA-ALE and MT@PLGA-ALE groups, whereas abundant mineralized nodules are observed in the BPs@PLGA-ALE+NIR and BPs/MT@PLGA-ALE+NIR groups. The semiquantitative analysis reveals that the level of extracellular matrix (ECM) mineralization in the BPs/MT@PLGA-ALE+NIR group is the highest (Figure 4e). The immunofluorescence staining result shows that OCN is highly expressed in the cells treated by MT@PLGA-ALE, BPs@PLGA-ALE+NIR and BPs/MT@PLGA-ALE+NIR, among which the BPs/MT@PLGA-ALE+NIR group shows the highest OCN expression (Figure 4f,g). Overall, the BPs/MT@PLGA-ALE+NIR group is superior in promoting osteogenesis in vitro.

2.5. In Vivo Bone Targeting Capability and Photothermal Effects

The bone targeting characteristics of BPs/MT@PLGA-ALE NSs is crucial to fracture healing under osteoporotic conditions. An osteoporotic fracture mice model is established by ovariectomy (OVX) and subsequent femoral fracture is created on the left femur at 4 weeks post-operation. ALE is one of the most widely utilized bone-binding ligands owing to its high binding affinity to HA.[18a] The molecular structure of ALE shows bidentate binding involving the two phosphonates, an −OH in the R1 side group and a nitrogen in the R2 side group, endow it with greater binding affinity to HA.[27] Since ALE is the functional component designed for bone targeting, the fluorescent Cy7-labeled PLGA-ALE NSs (targeted group) are intravenously administrated to the osteoporotic fracture mice with free Cy7 dye in PBS (no NSs group) and Cy7-labeled PLGA NSs (non-targeted group) as the control. The biodistributions in vivo are tracked by fluorescent imaging (**Figure 5**a). After 4 h of intravenous administration, only the Cy7-labeled PLGA-ALE NSs exhibit high accumulation at the predilection sites of osteoporosis like upper and lower extremities and spine (Figure 5b). Moreover, increased retention of fluorescence can be observed from the fracture sites of the left femurs (marked by green circles). Bone microenvironment is rich in HA, particularly the sites of metastatic lesions like bone resorption and fracture regions, where the bone turnover is high.[28] Therefore, PLGA-ALE NSs show a higher accumulation in these active sites. Quantification of total radiant efficiency of the image confirms that the Cy7-labeled PLGA-ALE NSs are better retained at the sites of fracture and osteoporotic predilections compared to the control (Figure 5c), indicating that functionalization of PLGA with ALE endow the PLGA-ALE NSs with the good bone targeting capability.

The photothermal characteristics of the BPs/MT@PLGA-ALE NSs is assessed in vivo by subjecting the experimental mice to NIR irradiation and monitoring the temperature of the fracture sites by an infrared camera. As shown in Figure 5d, the temperature rises at the fracture sites in the mice receiving BPs/MT@PLGA-ALE NSs is more significant than that of the PLGA-ALE group and PBS control group under the same NIR irradiation condition (808 nm, 0.7 W cm^{-2}, 15 min). The temperature at the fracture sites treated with the BPs/MT@PLGA-ALE NSs reach 45 °C after NIR irradiation for 10 min (Figure 5e) but in contrast, the final temperature of PLGA-ALE group increases to ≈37 °C and the PBS control group only reaches ≈35 °C after irradiation for 15 min. It has been reported that mild heat stimulation at 40–45 °C can enhance cell proliferation and regenerate bone tissues.[13a] However, the hyperthermia over 50 °C will denature proteins and disrupt the cell membranes causing harm to normal cells.[29] Hence, the maximum temperature is controlled to be 45 °C at the fracture sites. The BPs/MT@PLGA-ALE NSs are demonstrated for the good bone targeting capability and photothermal effects.

2.6. In Vivo Osteoporotic Fracture Healing and Alleviation of Osteoporosis

Encouraged by the suppression of osteoclastogenesis and promotion of osteogenesis by the BPs/MT@PLGA-ALE NSs in vitro in conjunction with desirable bone targeting and photothermal capacities, the therapeutic effects of BPs/MT@PLGA-ALE NSs are evaluated using an osteoporotic fracture mice model. The osteoporotic fracture mice are divided randomly into 5 groups as follows: 1) 10 mg kg^{-1} normal saline as the control group, 2) 10 mg kg^{-1} PLGA-ALE NSs, 3) 10 mg kg^{-1} MT@PLGA-ALE NSs, 4) 10 mg kg^{-1} BPs@PLGA-ALE NSs+NIR irradiation, and 5) 10 mg kg^{-1} BPs/MT@PLGA-ALE NSs+NIR irradiation. In the groups involving NIR irradiation, the fracture sites are irradiated with an 808 nm laser (0.7 W cm^{-2}, 10 min) under anesthesia 4 h after administration and continued at weekly intervals thereafter. X-ray imaging is performed at 3 days, 4 weeks, 8 weeks, and 12 weeks after fracture surgery and some of the mice are sacrificed at 4 weeks, 8 weeks and 12 weeks post-operation for further evaluation (**Figure 6**a).

As shown in Figure 6b, a tendency to back out of intramedullary pin can be observed from the control group (marked by red circle) but it is not noticeable from the other groups. Compared to the control group, the fracture gaps of the mice in the MT@PLGA-ALE, BPs@PLGA-ALE+NIR and BPs/MT@PLGA-ALE+NIR groups decrease significantly at 4 weeks post-surgery

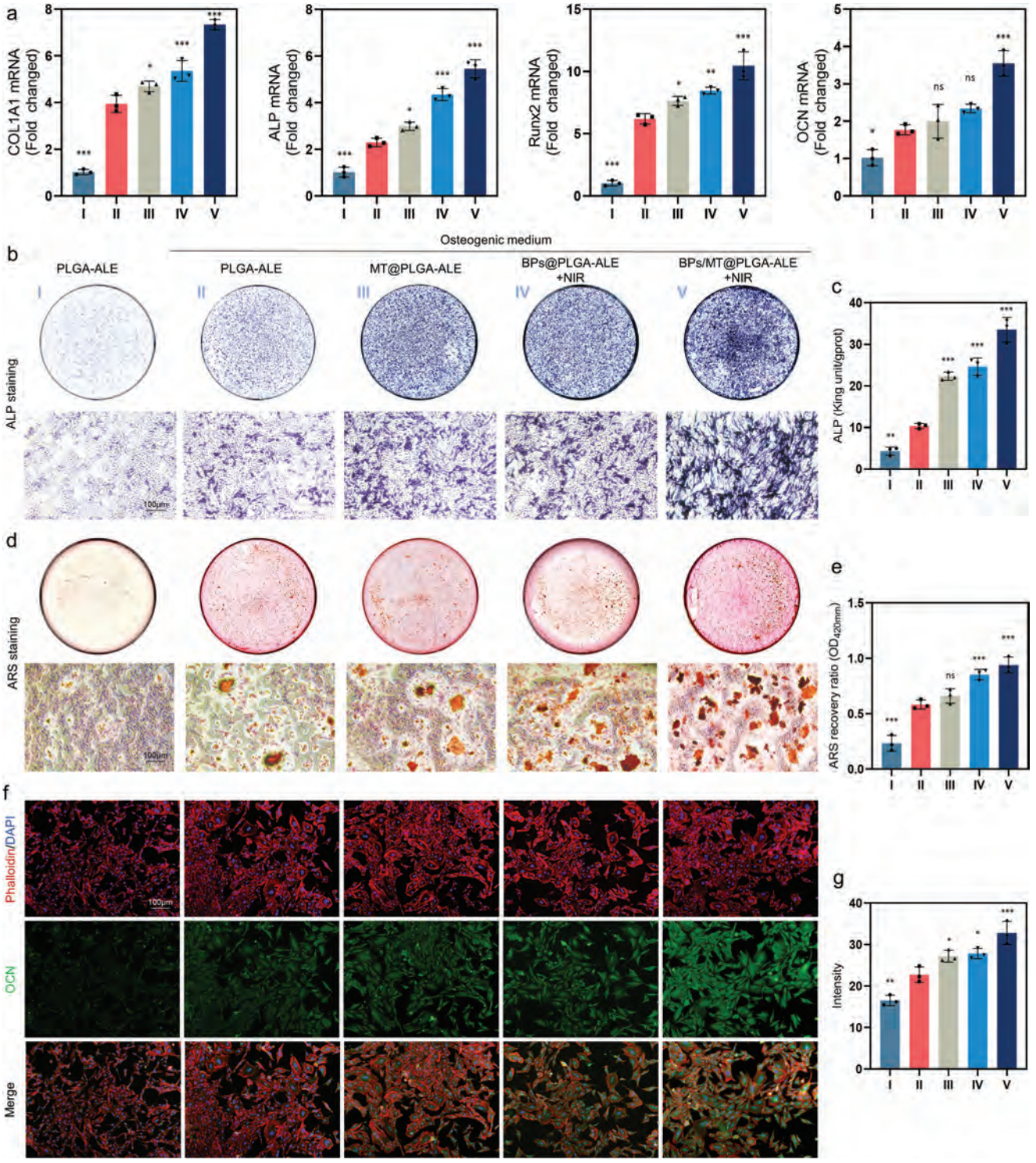

Figure 4. In vitro osteogenic differentiation of the MC3T3-E1 cells after different treatments (I: PLGA-ALE, II: PLGA-ALE + Osteogenic induction, III: MT@PLGA-ALE + Osteogenic induction, IV: BPs@PLGA-ALE+NIR + Osteogenic induction, V: BPs/MT@PLGA-ALE+NIR + Osteogenic induction). a) Gene levels of COL1A1, ALP, Runx2, and OCN; b) ALP staining; c) Quantitative evaluation of ALP activities; d) Alizarin red S staining; e) Semiquantitative evaluation of ECM mineralization; f) Immunofluorescent staining of OCN (green); g) Semiquantitative evaluation of OCN ($n = 3$ per group, * denotes $p < 0.05$, ** denotes $p < 0.01$, and *** denotes $p < 0.001$ compared to the PLGA-ALE + Osteogenic induction group).

(marked by red arrows). Moreover, the fracture line becomes blurred and bone remodeling takes place subsequently, especially in the BPs/MT@PLGA-ALE+NIR group. The delayed-union or non-union rates are 33.3%, 20.0%, and 6.7% for

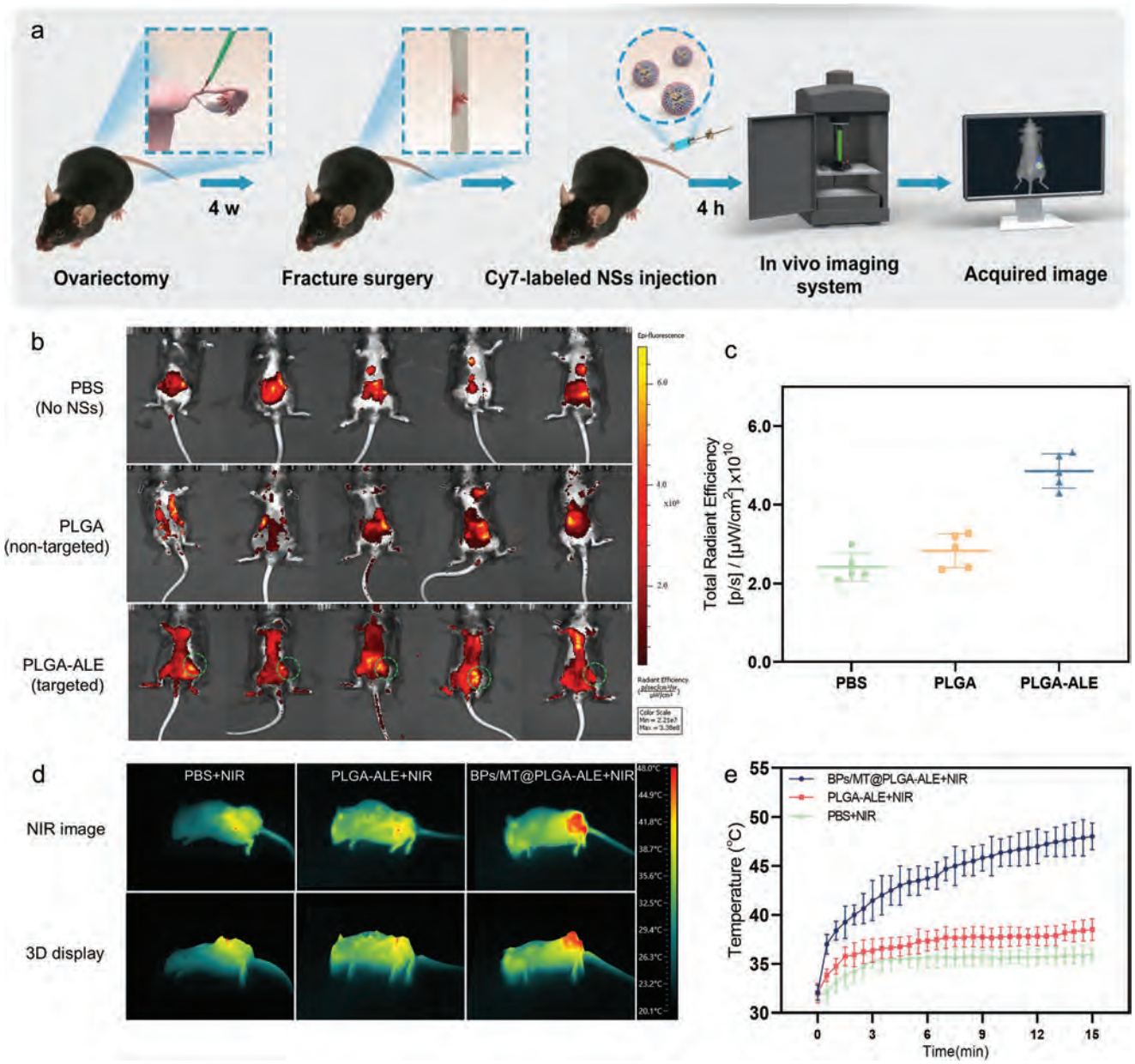

Figure 5. In vivo evaluation of the bone targeting properties and photothermal effects. a) Schematic illustration of the animal experiments; b) Whole-body fluorescent imaging of the experimental mice 4 h after intravenous administration of free Cy7 dye in PBS, Cy7-labeled PLGA NSs, and Cy7Cy7-labeled PLGA-ALE NSs (n = 5 per group, green circles indicate the fracture sites); c) Total fluorescence quantified in the region of interest of the whole-body fluorescent images shown in (b); d) Photothermal properties of different groups in vivo (n = 3 per group); e) NIR-induced temperature changes at the fracture sites of different mice.

the control group, PLGA-ALE group and MT@PLGA-ALE group, respectively, and all the fractures are united in the BPs/MT@PLGA-ALE+NIR group (Figure 6c). Meanwhile, the fracture healing scores of different groups evaluated from the X-ray images show that the BPQDs/MT@PLGA-ALE+NIR group fares the best (Figure 6d).

At 4 weeks, 8 weeks, and 12 weeks post-surgery, micro-CT scanning and 3D reconstruction of the osteoporotic fracture sites are carried out and the images of different groups are presented in Figure 6e. As marked by red rectangles in the images, the fracture line is clear and sharp in the control and PLGA-ALE group after 4 weeks. In contrast, blurred fracture lines and bone remodeling are observed from the MT@PLGA-ALE, BPs@PLGA-ALE+NIR, and BPs/MT@PLGA-ALE+NIR groups, indicating enhanced bone fracture healing. The mice receiving BPs/MT@PLGA-ALE NSs and NIR irradiation show the best therapeutic effects of bone fracture healing (Figure 6e). The quantitative analysis of the bone parameters reveals that both the callus mineral bone density (BMD) and bone volume per total volume (BV/TV) are the highest in the BPs/MT@PLGA-ALE+NIR group at all 3 time points (Figure 6f,g). Meanwhile, the right femurs of the mice without fracture are harvested

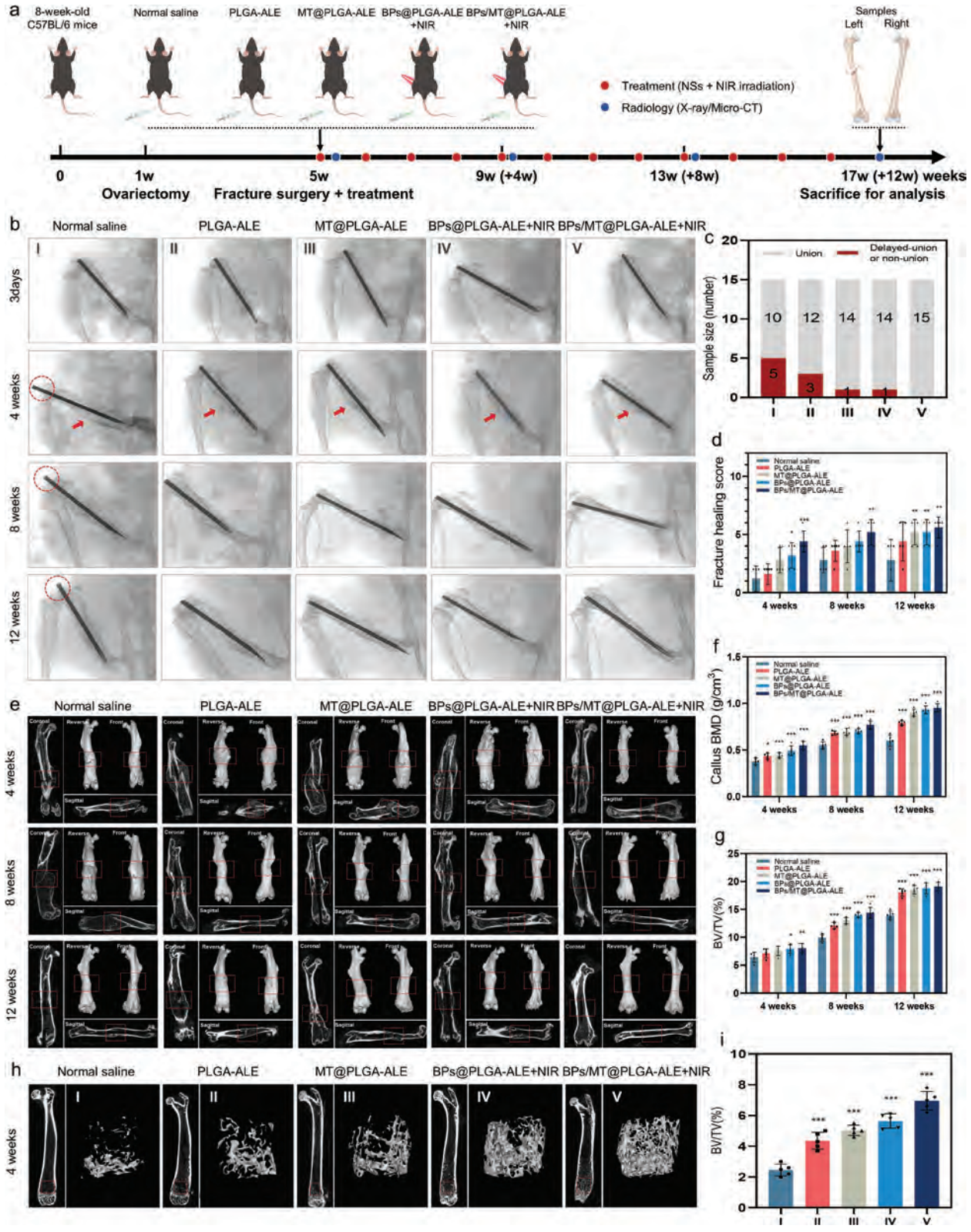

Figure 6. In vivo evaluation of osteoporotic fracture healing and alleviation of osteoporosis after different treatments. a) Schematic illustration of the animal experiments; b) X-ray images of the osteoporotic fracture sites (Red arrows indicate fracture gaps and red circles indicate back out of intramedullary pin); c) Delayed-union and non-union frequencies; d) Fracture healing scores; e) Representative images of micro-CT and 3D reconstruction of the osteoporotic fracture sites; f,g) BMD and BV/TV in the callus areas; h) Representative images of micro-CT and 3D reconstruction of osteoporosis; i) BV/TV in the regions above the distal femoral growth plate ($n = 5$ per group, * denotes $p < 0.05$, ** denotes $p < 0.01$, and *** denotes $p < 0.001$ compared to the normal saline group).

to assess the therapeutic effects on osteoporosis. As shown in Figure 6h, serious loss of the trabecular bone structure in regions above the distal femoral growth plate is observed from the control group, but this degenerative change can be prevented in the modified groups, especially by the treatment of BPs/MT@PLGA-ALE NSs with NIR irradiation. The highest BV/TV ratio is observed from the BP/MT@PLGA-ALE+NIR group (Figure 6i). These results indicate that the administration of BPs/MT@PLGA-ALE NSs combined with NIR irradiation produces superior therapeutic effects on osteoporotic fracture healing and alleviation of osteoporosis.

To further investigate the effects of different treatments on osteoporotic fracture healing, the harvested femoral samples are subjected to histological staining at 4 weeks, 8 weeks, and 12 weeks post-surgery. The H&E staining images of fractured femurs after different treatments show that cortical bone is thinner in the control and PLGA-ALE groups, and typical bone non-union with evident fracture gaps is observed from the control group after 12 weeks (marked by red arrow, **Figure 7**a). In comparison, the MT@PLGA-ALE, BPs@PLGA-ALE+NIR, and BPs/MT@PLGA-ALE+NIR groups show thicker cortical bone and better bone union, indicating better osteogenesis. The quantitative results reveal that the largest callus width can be detected in the BPs/MT@PLGA-ALE+NIR group (Figure 7b). H&E staining of the distal femoral condyle is performed and the amount of cancellous bone is the lowest in the control group and the highest in the BPs/MT@PLGA-ALE+NIR group (Figure 7c). Consistently, the trabecular areas in the osteoporotic femoral condyle increase the most after the treatment of BPs/MT@PLGA-ALE NSs and NIR irradiation (Figure 7d). Furthermore, the number of TRAP-positive cells in the fractured femurs and osteoporotic femoral condyles of the MT@PLGA-ALE, BPs@PLGA-ALE+NIR, and BPs/MT@PLGA-ALE+NIR groups decreases significantly compared to the control group, especially at 4 weeks post-surgery (Figure 7e–h). Masson staining shows that the blue-stained new bone tissues and red-stained cancellous bone are obvious in the modified groups indicative of increased calcification, maturation, and remodeling of new bone tissues (Figure 7i–l). Therefore, the BPs/MT@PLGA-ALE NSs combined with NIR irradiation show the greatest potential in post-operative treatment of osteoporotic fracture and osteoporosis.

2.7. Mechanisms of Regulation of Bone Homeostasis

To elucidate the mechanisms of BPs/MT@PLGA-ALE NSs and NIR irradiation on regulating bone homeostasis, RNA sequence analysis is carried out.[30] The MC3T3-E1 cells are incubated with PLGA-ALE and BPs/MT@PLGA-ALE NSs and subjected to osteogenic induction with or without NIR irradiation. After 3 days, the total RNA are extracted for transcriptome sequencing. The volcano map of differentially expressed genes (DEGs) shows that 908 DEGs are up-regulated and 824 DEGs are down-regulated in the BPs/MT@PLGA-ALE+NIR group compared to the the PLGA-ALE group (**Figure 8**a). A heat map is generated to present the different expression of DEGs in these two groups (Figure 8b) and principal component analysis (PCA) reveals that the samples of these two groups meet the requirements of quality control (Figure 8c). The sequencing data are further analyzed with gene ontology (GO) enrichment to determine the difference in the biological functions between these two groups. It is evident that the apoptotic process is regulated in the BPs/MT@PLGA-ALE+NIR group (Figure 8d). The Kyoto encyclopedia of genes and genomes (KEGG) enrichment analysis is performed to further explore the underlying signaling pathways. As shown in Figure 8e, the expression of tumor necrosis factor (TNF) and p53 signaling pathways are down-regulated in the BPs/MT@PLGA-ALE+NIR group (Figure 8e). Consistent with the KEGG analysis, gene set enrichment analysis (GSEA) reveals that the BPs/MT@PLGA-ALE group negatively correlates with the above two pathways (Figure 8f). The differential expression of osteoblast-related biomarkers and genes in TNF and apoptosis signaling pathways are displayed in the correlated heat map (Figure S13, Supporting Information). The TNF and p53 signaling pathways are important participants in apoptosis signaling pathway. To further verify whether the effect of BPs/MT@PLGA-ALE NSs on osteoporotic fracture healing is dependent on apoptosis signaling pathway, ABT-737, a potent apoptosis inducer, is used for the co-treatment of MC3T3-E1 cells. The qRT-PCR results show that the gene levels of B-cell lymphoma-2 (Bcl2) is decreased and gene levels of TNF receptor superfamily member 6 (Fas) and cysteinyl aspartate specific proteinase 7 (Caspase 7) are increased by the administration of ABT-737 (Figure S14, Supporting Information). However, the BPs/MT@PLGA-ALE+NIR group exert a rescue effect on these apoptosis-related genes. The results suggest that the BPs/MT@PLGA-ALE NSs combined with NIR irradiation produce positive effects on bone formation by inhibiting TNF and apoptosis signaling pathways.

The RAW264.7 cells in the PLGA-ALE group and BPs/MT@PLGA-ALE+NIR group are also investigated by transcriptome sequencing after RANKL induction for 3 days. The volcano map and heat map show that 16 DEGs are up-regulated and 104 DEGs are down-regulated in the BPs/MT@PLGA-ALE+NIR group compared to the PLGA-ALE group (Figure 8g,h). PCA shows that the samples of the two groups meet the requirements of quality control (Figure 8i). As shown in Figure 8j, enhancement of bone remodeling and oxidative stress response can be detected from the BPs/MT@PLGA-ALE+NIR group. KEGG enrichment analysis demonstrates that the expression of osteoclast differentiation, necroptosis, apoptosis, TNF, and nucleotide oligomerization domain (NOD)-like receptor signaling pathways are down-regulated in the BPs/MT@PLGA-ALE+NIR group (Figure 8k). GSEA validates that the BPs/MT@PLGA-ALE+NIR group correlates negatively with the necroptosis and TNF signaling pathways (Figure 8l). The differential expression of osteoclast-related biomarkers and genes in the TNF and NOD-like receptor signaling pathways are presented in the correlated heat map (Figure S15, Supporting Information). In addition, qRT-PCR results confirm that in vitro treatment with BPs/MT@PLGA-ALE+NIR group can reduce the gene levels of Nlrc4, Caspase 1 and Il-18 under the intervention of 100 ng ml^{-1} LPS and 5 mM ATP (Figure S16, Supporting Information). The results disclose that BPs/MT@PLGA-ALE NSs combined with NIR irradiation have promising potential in regulating bone homeostasis by modulating the TNF and cell death-related signaling pathways.

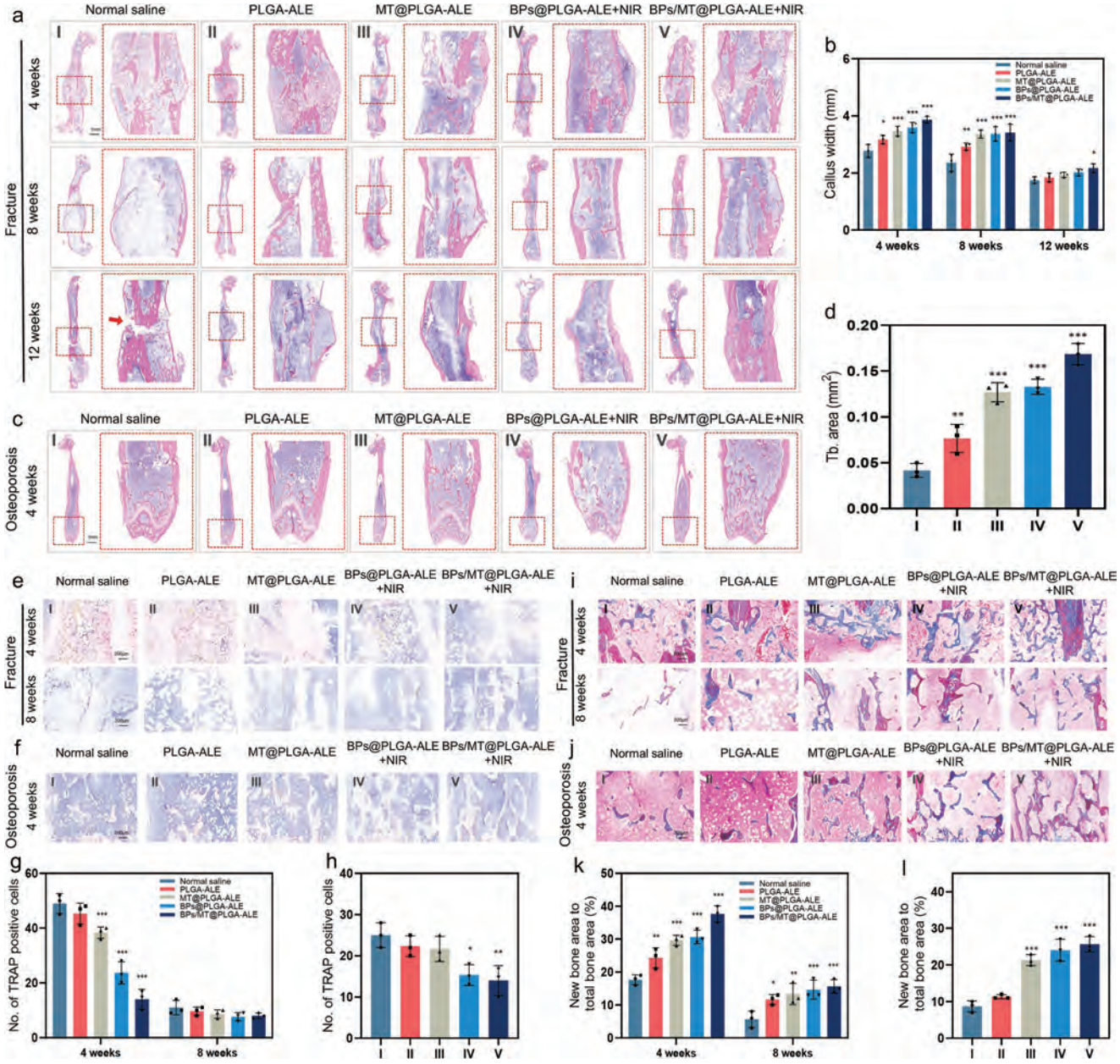

Figure 7. a) Typical gross view of the fractured femurs after H&E staining at 4 weeks, 8 weeks, and 12 weeks after operation (Red arrow indicates bone non-union); b) Callus width evaluated at 4 weeks, 8 weeks, and 12 weeks post-operation; c) Gross view of the femoral condyles with H&E staining at 4 weeks post-operation; d) Quantitative evaluation of the trabecular areas at 4 weeks post-operation; e) Magnified view of the fractured femurs with TRAP staining at 4 weeks and 8 weeks post-operation; f) Magnified view of the femoral condyles with TRAP staining at 4 weeks post-operation; g) Quantitative evaluation of the TRAP-positive cells in the fractured femurs at 4 weeks and 8 weeks post-operation; h) Quantitative evaluation of the TRAP-positive cells in the femoral condyles at 4 weeks post-operation; i) Magnified view of the fractured femurs with Masson staining at 4 weeks and 8 weeks post-operation; j) Magnified view of the femoral condyles with Masson staining at 4 weeks post-operation; k) Quantitative evaluation of the ratio of new bone area to total bone area in the fractured femurs at 4 weeks and 8 weeks post-operation; l) Quantitative evaluation of the ratio of new bone area to total bone area in the femoral condyles at 4 weeks post-operation ($n = 3$ per group, * denotes $p < 0.05$, ** denotes $p < 0.01$, and *** denotes $p < 0.001$ compared to the normal saline group).

3. Conclusion

A multifunctional nanoplatform is designed by integrating BPs and MT into the ALE-conjugated PLGA NSs to treat osteoporotic bone fracture. BPs take part in the photothermal treatment upon NIR irradiation and encapsulation of BPs into PLGA enhances the stability, consequently facilitating osteogenesis by means of mild hyperthermia with minimal adverse effects. The incorporated MT is capable of modulating bone metabolism by suppressing osteoclastogenesis and promoting osteogenesis. By modifying PLGA with ALE, the NSs possess the bone targeting capacity to achieve better therapeutic effects.

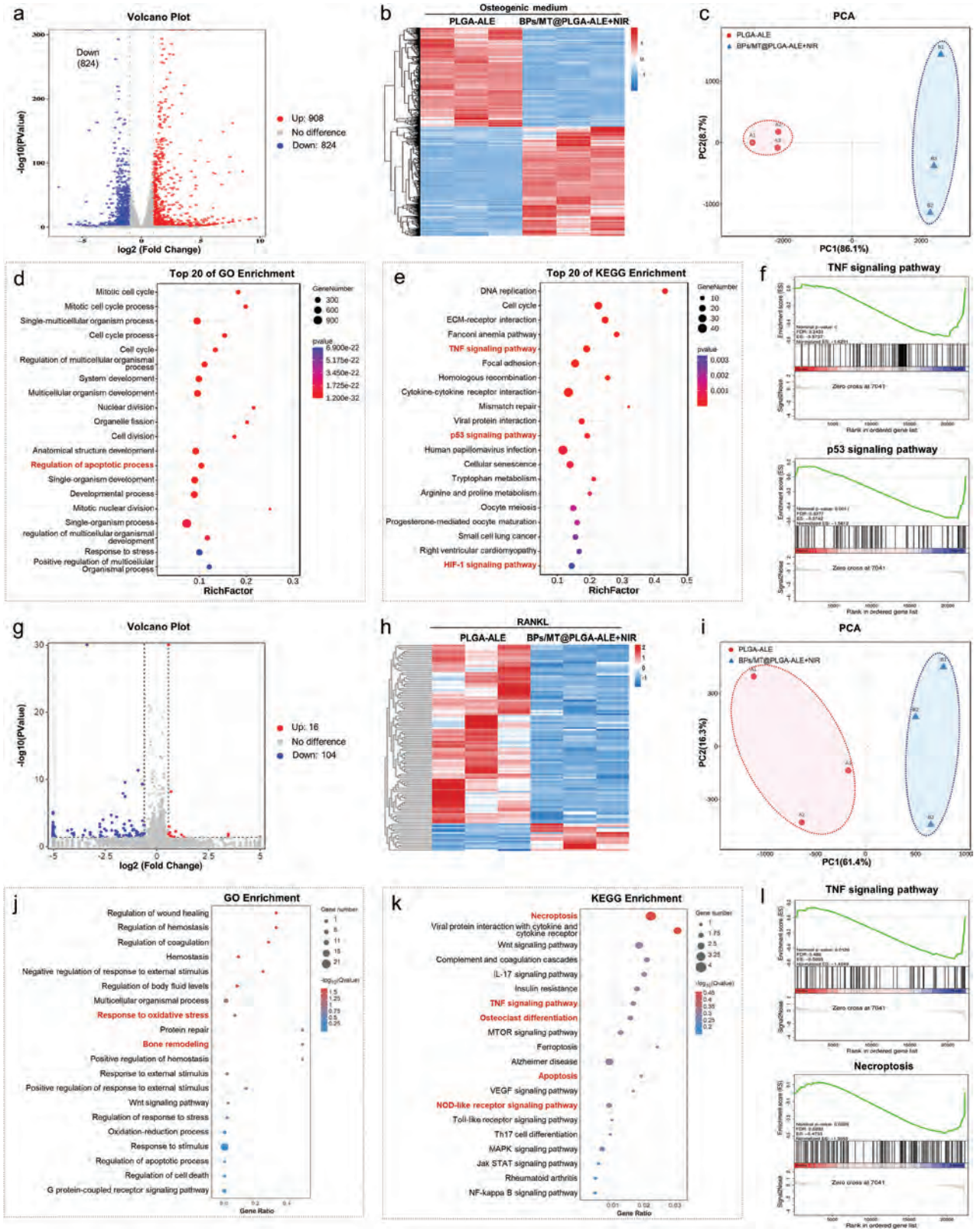

Figure 8. Transcriptome sequencing analysis of the cells in the PLGA-ALE and BPs/MT@PLGA-ALE+NIR groups. a) Volcano map of DEGs in the MC3T3-E1 cells after osteogenic induction; b) Heat map of DEGs; c) PPCA of the samples in the two groups; d,e) GO and KEGG enrichment analysis of DEGs; f) GSEA analysis of TNF and p53 signaling pathways; g) Volcano map of DEGs in the RAW264.7 cells after RANKL induction; h) Heat map of DEGs; i) PCA of the samples in the two groups; j,k) GO and KEGG enrichment analysis of DEGs; l) GSEA analysis of the TNF signaling pathway and necroptosis.

Overall, this therapeutic nanoplatform can restore the balance of bone homeostasis under osteoporotic conditions by modulating the TNF and cell death-related signaling pathways. The strategy is effective in accelerating osteoporotic fracture healing and the results provide insights into the design and development of nanomaterials for the treatments of bone diseases.

4. Experimental Section

Materials: The >99.99% pure BP powders were purchased from Mophos and 1-Methyl-2-pyrrolidinone (NMP) (99.9%, electronic level), PLGA (actide:glycolide = 50:50, MW: 30000–60000), N-(3-dimethylaminopropyl)-N'-ethylcarbodiimide hydrochloride (EDC), N-Hydroxysuccinimide (NHS), dimethyl sulfoxide (DMSO), MT and acetonitrile were obtained from Aladdin Reagents (Shanghai, China). ALE, acetic acid, acetone, diethyl ether, and DCM were bought from Sinopharm Chemical Reagent Co. Ltd (Shanghai, China). PVA (MW: 9000–10000) was purchased from Sigma-Aldrich Co. USA and PBS was obtained from Cytiva. Cell culture dishes and cell culture plates were obtained from NEST Biotechnology Co. Ltd (Wuxi, China). All the chemicals were used as received without purification and Millipore™ Milli-Q water (resistivity >18 MΩ cm^{-1} at 25 °C) was used throughout the experiments.

Preparation of BPs: 100 mg of the bulk BP powders were dispersed in 100 mL of NMP and sonicated with a probe using a power of 1200 W. The mixture was sonicated overnight in an ice bath using a power of 200 W. The dispersion was centrifuged for 10 min at 10000 revolutions per minute (rpm) and the supernatant containing the BPs was decanted gently. The obtained BPs were dispersed in NMP for storage.

Synthesis of the PLGA-ALE polymer: ALE (1.1 g) were dissolved in 11.1 mL of 10% aqueous acetic acid and lyophilized to obtain the free acid form and then, 0.5 g of PLGA was dissolved in 15 mL of acetone and activated by 25 mg EDC and 27 mg NHS overnight at room temperature.[31] The by-product after activation was removed with a syringe filter (0.45 µm pore size) and the activated PLGA was precipitated in cold diethyl ether and dried at 25 °C for 4 h in a vacuum oven. Finally, 0.5 g of the activated PLGA and 7 mg of the treated ALE were dissolved in a mixture containing 47.5 mL DMSO and 2.5 mL water and stirred for 24 h at room temperature. The PLGA-ALE conjugated polymer was precipitated using a copious amount of cold diethyl ether and water, dried in a vacuum oven at 25 °C for 4 h, and stored at 4 °C.

Fabrication of BPs/MT@PLGA-ALE NSs: The BPs/MT@PLGA-ALE NSs were prepared by an oil-in-water emulsion solvent evaporation method. In brief, 20 mL of the BPs suspension in NMP (65 µg mL^{-1}) were centrifuged for 20 min at 12000 rpm and the precipitate was redispersed in 0.5 mL of DCM. At the same time, 0.5 mL DCM containing 25 mg of MT was added to the suspension. After probe sonication (130 W) for 5 min (periods of 5 s and intervals of 2 s), the mixture was dispersed in 10 mL of the 1% (w/v) PVA aqueous solution containing 0.0116 g MT and sonicated for another 5 min. The emulsion was stirred overnight at room temperature to evaporate the residual DCM. Finally, the BPs/MT@PLGA-ALE NSs suspension were centrifuged in ultrafiltration centrifuge tubes at 6500 rpm for 10 min, washed twice with water to remove the superfluous BPs, MT, and PVA, and re-suspended in the aqueous solution. The PLGA-ALE NSs, MT@PLGA-ALE NSs, and BPs@PLGA-ALE NSs were fabricated by the same protocol but without the corresponding ingredients.

Characterization: The ^{1}H NMR spectra were acquired on the AVANCE III 400 M spectrometer (Bruker, Germany) and the FTIR spectra were obtained on the Frontier™ Fourier transform infrared spectrometer (PerkinElmer, USA). SEM and EDS were conducted on the SUPRA 55 field-emission scanning electron microscope (Carl Zeiss, Germany). The size and zeta potentials of the different nanospheres were determined on the Zetasizer Nano ZS (Malvern, UK). TEM images were acquired on a JEM-F200 emission transmission electron microscope (JEOL, Japan). Raman scattering was performed on the Jobin-Yvon Lab Ram HR VIS high-resolution confocal Raman microscope (HORIBA, France) with the 633 nm laser as the excitation source. The UV–visible–NIR absorption spectra were obtained from a quartz cuvette with a 1 cm path length on a TU-1810 spectrophotometer (Persee, China). The photothermal properties were investigated employing a KS-810F-8000 continuous fiber-coupled semiconductor diode laser (Kai Site Electronic Technology, China) as the light source. The samples were irradiated with the 808 nm NIR laser at a power density of 1.5 W cm^{-2} for 15 min and the temperature changes was monitored by a Ti27 infrared thermal imaging camera (Fluke, USA). To measure the loaded amounts of BPs and MT, the BPs/MT/PLGA-ALE NSs were dissolved in acetonitrile and centrifuged at 15000 rpm for 30 min. The supernatant was used to determine the content of MT by monitoring the absorbance at 277 nm in the UV–visible–NIR absorption spectra and the precipitate was used to determine the content of BPs by ICP-AES (PerkinElmer, USA). The loading content was calculated by LC% = (weight of MT or BPs in NSs)/(weight of NSs) × 100%.

Cell Culturing and Differentiation: The murine macrophage cell line RAW264.7 and murine pre-osteoblast cell line MC3T3-E1 were used in the study. The RAW264.7 cells were obtained from the Chinese Academy of Sciences (Shanghai, China) and MC3T3-E1 cells were provided by the American Type Culture Collection (ATCC, USA). The RAW264.7 and MC3T3-E1 cells were cultivated in the Dulbecco's Modified Eagle Medium (DMEM) containing 10% fetal bovine serum (FBS) and penicillin/streptomycin antibiotics under 5% CO_2 at 37 °C. To determine osteoclastic differentiation of RAW264.7 cells, the medium was DMEM supplemented with 10% FBS and 50 ng ml^{-1} RANKL and to study osteogenic differentiation of the MC3T3-E1 cells, the medium was DMEM supplemented with 10% FBS, 0.5 mM vitamin C, 0.1 µM dexamethasone, and 10 mM β-glycerophosphate. The cells in some experimental groups were exposed to the 808 nm laser irradiation for 10 min every 12 h.

Cell Viability Assay: The cytotoxicity of PLGA-ALE NSs, MT@PLGA-ALE NSs, BPs@PLGA-ALE NSs, and BPs/MT@PLGA-ALE NSs to RAW264.7 and MC3T3-E1 was evaluated by using a CCK-8 kit (Beyotime, China). Both cells were cultured on 96-well plates at a density of 5000 cells/well and different concentrations of PLGA-ALE NSs, MT@PLGA-ALE NSs, BPs@PLGA-ALE NSs, and BPs/MT@PLGA-ALE NSs were then added and cultivated for 24 and 72 h. Afterward, the cells were rinsed and incubated with 100 µl of DMEM containing 10 µl of the CCK-8 solution for 1 h at 37 °C and the absorbance at 450 nm was monitored.

Live/Dead Staining Assay: Briefly, both kinds of cells were seeded on coverslips on 24-well plates at a density of 30000 cells/well. The cells were incubated with 12.5 µg ml^{-1} PLGA-ALE NSs, MT@PLGA-ALE NSs, BPs@PLGA-ALE NSs, and BPs/MT@PLGA-ALE NSs for 72 h with or without periodic NIR irradiation. The live/dead staining assay was conducted using a commercially LIVE/DEAD® viability assay kit (Introvegen, USA) according to the manufacturer's instructions. The concentration of Calcein AM (green) used in live staining was 2 µM and that of propidium iodide (PI, red) in dead staining was 4 µM. Finally, the stained coverslips were observed under a LSM510 fluorescence microscope (Zeiss, Germany).

Western Blot Analysis: The proteins in the cells after different treatments were extracted by the radio immunoprecipitation assay and the supernatant fraction was kept after centrifugation. The bicinchoninic acid (BCA) kit was utilized to determine the concentration of proteins. 20 µg of the proteins were separated by SDS-PAGE and transferred to a nitrocellulose membrane which was sealed with a blocking buffer and incubated with the primary antibodies, including antibodies against MMP9 (1:1000 dilution, A0289, Abclonal, China), c-fos (1:1000 dilution, 2250S, Cell Signaling Technology, USA), Nfatc1 (1:1000 dilution, 8032S, Cell Signaling Technology, USA), TRAP (1:500 dilution, Ab2391, Abcam, UK), β-actin (1:10000 dilution, AC026, Abclonal, China), COL1A1 (1:1000 dilution, A16891, Abclonal, China), ALP (1:1000 dilution, DF4722, Affinity Biosciences, USA), Runx2 (1:1000 dilution, A2851, Abclonal, China), OCN (1:1000 dilution, orb1266, Biorbyt, UK), and corresponding secondary antibodies (1:5000 dilution, Beyotime, China). The protein bands were analyzed by the ChemiDoc gel imaging system (Bio-Rad, USA) and protein semi-quantification was performed using ImageJ (Bethesda, USA).

Quantitative Real-Time PCR Assay: The total RNA in the cells after different treatments was isolated using TRIzol reagent (Beyotime, China) and complementary DNA (cDNA) was generated from isolated RNA by reverse transcription. The cDNA was amplified in a CFX96™ real-time PCR system (Bio-Rad, USA) and the primers of the target genes are listed in Table S2 (Supporting Information).

Osteoclast Formation Assay: The RAW264.7 cells were seeded on 48-well plates with a density of 30000 cells/well. They were subjected to different treatments and induced with 50 ng ml^{-1} RANKL for 5 days. TRAP staining was performed according to the manufacturer's protocol (Bizhong Bio, China). The TRAP-positive osteoclasts (≥3 nuclei) were examined by bright microscopy (Zeiss, Germany) and semi-quantification was performed using ImageJ (Bethesda, USA).

Bone Resorption Assay: The RAW264.7 cells after different treatments were seeded on bovine bone slices (JoyTech Biotechnology, China) and induced with 50 ng ml^{-1} RANKL for 1 week. The cells were removed from the bovine bone slices using a water bath sonicator. After dehydration with gradient ethanol, the samples were dried by critical point drying, sputter-coated with gold, and examined by the FEI Quanta 250 scanning electron microscope (Hillsboro, USA). The resorption area was quantitated using ImageJ (Bethesda, USA).

ALP Staining: The MC3T3-E1 cells were seeded on 24-well plates at a density of 40000 cells/well. They were subjected to different treatments and cultured in the osteogenic medium for 7 days. The cells were fixed with 4% paraformaldehyde and dark-incubated with the BCIP/NBT working solution (Beyotime, China). The ALP activity was evaluated using an Alkaline Phosphatase quantification Kit (Jiancheng Bioengineering Institute, China) according to the manufacturer's instructions and the absorbance at 520 nm was measured.

Alizarin Red S Staining: The MC3T3-E1 cells were seeded on 24-well plates at a concentration of 30000 cells/well. They were subjected to different treatments and cultured in the osteogenic medium for 21 days. The cells were fixed with 95% ethanol and dark-incubated with the 0.1% ARS staining solution (pH 4.2, Beyotime, China). The stained calcium nodules were examined under a bright microscope (Zeiss, Germany). The calcium nodules were dissolved by 5% perchloric acid and the optical density was measured at a wavelength of 420 nm.

Cell Immunofluorescence Staining: The cells after different treatments were fixed with 4% paraformaldehyde and permeabilized with 0.2% Triton X-100 (Beyotime, China). The primary OCN antibody (1:100 dilution, orb1266, Biorbyt, UK) was added and incubated overnight and the cells were stained with the corresponding secondary fluorescent antibody (1:1000 dilution, Alexa Fluor® 488, Abcam, UK). The cells were co-stained with phalloidin (Yeasen, China) and DAPI (Beyotime, China). The fluorescent stained cells were observed under a fluorescence microscope (Zeiss, Germany) and the intensity was evaluated using ImageJ (Bethesda, USA).

Animals, Osteoporotic Fracture Induction, and Experimental Groups: The animal experiments were authorized by the Animal Ethics Committee of the First Affiliated Hospital of Soochow University (approval number: SUDA20220130A02). A total of 75 ten-week-old female C57BL/6 mice were used. Bilateral OVX was performed to induce osteoporosis in the experimental mice under 60 mg kg^{-1} pentobarbital sodium anesthesia. After 4 weeks, femoral fracture was carried out on the left femur. The surgical site was disinfected and the skin was cut from the outside of the knee to the middle of leg. A transverse fracture was made at the middle part of the femur and a 23G needle was inserted into the marrow cavity to fix the fracture. The incision was sutured and penicillin G was administered.

Seventy five mice were randomly divided into 5 experimental groups (n = 15/group): control group (OVX + fracture + PBS treatment), PLGA-ALE group (OVX + fracture + 10 mg kg^{-1} PLGA-ALE treatment), MT@PLGA-ALE group (OVX + fracture + 10 mg kg^{-1} MT@PLGA-ALE treatment), BPs@PLGA-ALE+NIR group (OVX + fracture + 10 mg kg^{-1} BPs@PLGA-ALE + NIR treatment), and BPs/MT@PLGA-ALE+NIR group (OVX + fracture + 10 mg kg^{-1} BPs/MT@PLGA-ALE + NIR treatment). Each group was administered weekly and the fracture sites in the mice of the BPs@PLGA-ALE+NIR and BPs/MT@PLGA-ALE+NIR groups were illuminated with NIR light (808 nm, 0.7 W cm^{-2}) for 10 min weekly. Some of the mice in each group were sacrificed at 4, 8, and 12 weeks after fracture operation and the bilateral femurs were harvested to evaluate the therapeutic effects on osteoporotic fracture healing and alleviation of osteoporosis, respectively.

Photothermal Imaging: The photothermal efficiency of the PLGA-ALE NSs and BPs/MT@PLGA-ALE NSs was determined in vivo. The mice received intravenous administration of 10 mg kg^{-1} PLGA-ALE and BPs/MT@PLGA-ALE NSs, respectively and after 4 h, the fracture sites in the mice under anesthesia were irradiated with the 808 nm NIR laser for 15 min. An infrared thermal imaging camera (Guide infrared, China) was utilized to capture the real-time thermal images and the corresponding temperature variation was recorded.

In Vivo Biodistribution: The Cy7-labeled PLGA and PLGA-ALE NSs were prepared for live animal imaging. The PLGA and PLGA-ALE NSs were redispersed in 2 ml of deionized water (2 mg ml^{-1}) and 50 µl of DMSO with the 10% (w/w) Cy7 fluorescent agent were added under continuous stirring at room temperature overnight. The mixture was then centrifuged at 10000 rpm for 10 min to remove the loose Cy7 and obtain the Cy7-labeled NSs. In whole-body imaging, 0.5 mg of the Cy7-labeled NSs dispersed in PBS were intravenously injected and bioluminescence was monitored by the Lumina Series III in vivo imaging system (Caliper Life Sciences, USA).

Radiological Analysis: To evaluate fracture healing, X-ray imaging (SkyScan1176, Belgium) was performed at 3 days, 4, 8, and 12 weeks post-operation. Both the sizes of non-union and fracture healing scores were determined. The fracture healing scoring is quantified by the status of bone repair and growth of callus, and graded as follows: no callus with clear fracture line (score = 0); small amounts of low-density callus (score = 2); large amounts of high-density callus (score = 4); large amounts of callus with disappeared fracture line (score = 6). A high-resolution micro-CT system (SkyScan1176, Belgium) was utilized to determine osteoporosis and fracture healing of the femurs at 4, 8, and 12 weeks post-operation. The scanning parameters were as follows: 9 µm per layer at a voltage of 50 kV and current of 200 µA. Subsequently, 3D image reconstruction was conducted and the morphometric parameters including callus BMD and BV/TV were measured.

Histological Staining: The collected femurs were fixed in the 10% formalin-buffered solution for at least 48 h and decalcified with 10% EDTA for 1 month. The implanted needles were carefully removed and the specimens were embedded in paraffin wax and sectioned into 6 µm sections. Routine H&E staining was performed to evaluate the morphological changes of the tissues. The callus widths and trabecular areas in the fracture sites and distal femurs were determined. TRAP staining was performed and the number of TRAP-positive multinucleated osteoclasts in the selected regions were quantified. Masson staining was also performed to assess the presence of immature collagen and new bone formation. The ratio of the new bone area to total bone area in the region of interest was analyzed. The histological sections were visualized and observed by the Axio-Cam HRC microscope (Zeiss, Germany).

RNA Sequencing and Bioinformatics: The RAW264.7 cells with RANKL induction were treated with the PLGA NSs and BPs/MT@PLGA-ALE NSs + NIR irradiation. The MC3T3-E1 cells with osteogenic induction were treated with the PLGA NSs and BPs/MT@PLGA-ALE NSs + NIR irradiation. After 3 days, the cells in different groups were harvested and the total RNA was extracted by the TRIzol reagent (Beyotime, China) and quantified using a Nano Drop 2000 spectrophotometer. Transcriptome sequencing analysis was performed by Gene Denovo and Genewiz Co. Clean reads were aligned to the reference genes using Hisat2 software and fragments per kilobase per million mapped reads (FPKM) values were generated using the Cufflinks software. The difference between differential transcripts was evaluated by GO and KEGG enrichment analysis. The expression was considered statistically differential for genes with p values less than 0.05 and difference greater than 1.5. Unsupervised hierarchical clustering of differential transcripts was performed using a heat map format.

Statistical Analysis: All the data were represented as means ± standard deviation. The student's t-test was used to verify the significance of

differences between two groups and one-way ANOVA analysis was performed for multiple comparison. The GraphPad Prism 8.0 software was employed in the statistical analysis and statistical significance was defined as $p < 0.05$.

Supporting Information

Supporting Information is available from the Wiley Online Library or from the author.

Acknowledgements

K. Z., J. B., and W. C. contributed equally to this work. This work was financially supported by the National Natural Science Foundation of China (82072425, 82072498, 31922040, 81903057, 82172397, and 82272157), Shenzhen Science and Technology Research Funding (JCYJ20180507182637685 and JSGG20200225152648408), Natural Science Foundation of Jiangsu Province (BE2021650), Jiangsu Medical Research Project (ZD2022021), Youth Innovation Promotion Association of Chinese Academy of Sciences (2020353), Special Project of Diagnosis and 1372 Treatment Technology for Key Clinical Diseases in Suzhou (LCZX202003), Priority Academic Program Development of Jiangsu Higher Education Institutions (PAPD), City University of Hong Kong Donation Research Grant (DON-RMG 9229021), City University of Hong Kong Strategic Research Grant (SRG 7005505), City University of Hong Kong Donation Grant (9220061), Hong Kong PDFS-RGC Postdoctoral Fellowship Scheme (PDFS2122-1S08 and CityU 9061014), Hong Kong Health and Medical Research Fund (2120972 and CityU 9211320), and Key Laboratory of Orthopaedics of Suzhou (SZS2022017).

Conflict of Interest

The authors declare no conflict of interest.

Data Availability Statement

Research data are not shared.

Keywords

bone homeostasis, bone targeting, multifunctional nanospheres, near-infrared irradiation, osteoporotic fractures

Received: December 3, 2022
Revised: January 9, 2023
Published online: February 28, 2023

[1] I. R. Reid, *Nat. Rev. Endocrinol.* **2020**, *16*, 333.
[2] J. A. Cauley, D. Chalhoub, A. M. Kassem, G. E. H. Fuleihan, *Nat. Rev. Endocrinol.* **2014**, *10*, 338.
[3] J. A. Kanis, O. Johnell, A. Oden, I. Sembo, I. Redlund-Johnell, A. Dawson, C. De Laet, B. Jonsson, *Osteoporosis Int.* **2000**, *11*, 669.
[4] O. Johnell, J. A. Kanis, *Osteoporosis Int.* **2006**, *17*, 1726.
[5] N. C. Harvey, E. V. McCloskey, P. J. Mitchell, B. Dawson-Hughes, D. D. Pierroz, J. Y. Reginster, R. Rizzoli, C. Cooper, J. A. Kanis, *Osteoporosis Int.* **2017**, *28*, 1507.
[6] T. D. Rachner, S. Khosla, L. C. Hofbauer, *Lancet* **2011**, *377*, 1276.
[7] J. E. Compston, M. R. McClung, W. D. Leslie, *Lancet* **2019**, *393*, 364.
[8] a) J. E. Rossouw, G. L. Anderson, R. L. Prentice, A. Z. LaCroix, C. Kooperberg, M. L. Stefanick, R. D. Jackson, S. A. Beresford, B. V. Howard, K. C. Johnson, J. M. Kotchen, J. Ockene, *JAMA, J. Am. Med. Assoc.* **2002**, *288*, 321; b) D. M. Black, C. J. Rosen, *N. Engl. J. Med.* **2016**, *374*, 254.
[9] B. Z. Leder, *Curr. Osteoporosis Rep.* **2017**, *15*, 110.
[10] Z. Wan, P. Zhang, L. Lv, Y. Zhou, *Theranostics* **2020**, *10*, 11837.
[11] X. Yi, Q. Y. Duan, F. G. Wu, *Research (Wash D C)* **2021**, *2021*, 9816594.
[12] a) H. Chen, Z. Liu, B. Wei, J. Huang, X. You, J. Zhang, Z. Yuan, Z. Tang, Z. Guo, J. Wu, *Bioact. Mater.* **2021**, *6*, 655; b) Y. Li, Z. Liu, Y. Hou, G. Yang, X. Fei, H. Zhao, Y. Guo, C. Su, Z. Wang, H. Zhong, Z. Zhuang, Z. Guo, *ACS Appl. Mater. Interfaces* **2017**, *9*, 25098.
[13] a) L. Tong, Q. Liao, Y. Zhao, H. Huang, A. Gao, W. Zhang, X. Gao, W. Wei, M. Guan, P. K. Chu, H. Wang, *Biomaterials* **2019**, *193*, 30550998; b) Y. Wu, Q. Liao, L. Wu, Y. Luo, W. Zhang, M. Guan, H. Pan, L. Tong, P. K. Chu, H. Wang, *ACS Nano* **2021**, *15*, 17854.
[14] R. A. Doganov, E. C. O'Farrell, S. P. Koenig, Y. Yeo, A. Ziletti, A. Carvalho, D. K. Campbell, D. F. Coker, K. Watanabe, T. Taniguchi, A. H. Castro Neto, B. Ozyilmaz, *Nat. Commun.* **2015**, *6*, 6647.
[15] F. Munmun, P. A. Witt-Enderby, *J. Pineal Res.* **2021**, *71*, 12749.
[16] a) Z. Ping, Z. Wang, J. Shi, L. Wang, X. Guo, W. Zhou, X. Hu, X. Wu, Y. Liu, W. Zhang, H. Yang, Y. Xu, Y. Gu, D. Geng, *Acta Biomater.* **2017**, *62*, 362; b) Z. Ping, X. Hu, L. Wang, J. Shi, Y. Tao, X. Wu, Z. Hou, X. Guo, W. Zhang, H. Yang, Y. Xu, Z. Wang, D. Geng, *Acta Biomater.* **2017**, *51*, 513.
[17] M. S. Shive, J. M. Anderson, *Adv. Drug Delivery Rev.* **1997**, *28*, 5.
[18] a) L. E. Cole, T. Vargo-Gogola, R. K. Roeder, *Adv. Drug Delivery Rev.* **2016**, *99*, 12; b) H. Qiao, Z. Cui, S. Yang, D. Ji, Y. Wang, Y. Yang, X. Han, Q. Fan, A. Qin, T. Wang, X. P. He, W. Bu, T. Tang, *ACS Nano* **2017**, *11*, 7259.
[19] Z. Sun, H. Xie, S. Tang, X. F. Yu, Z. Guo, J. Shao, H. Zhang, H. Huang, H. Wang, P. K. Chu, *Angew. Chem., Int. Ed.* **2015**, *54*, 11526.
[20] R. Pignatello, E. Cenni, D. Micieli, C. Fotia, M. Salerno, D. Granchi, S. Avnet, M. G. Sarpietro, F. Castelli, N. Baldini, *Nanomedicine (Lond)* **2009**, *4*, 161.
[21] J. Shao, H. Xie, H. Huang, Z. Li, Z. Sun, Y. Xu, Q. Xiao, X. F. Yu, Y. Zhao, H. Zhang, H. Wang, P. K. Chu, *Nat. Commun.* **2016**, *7*, 12967.
[22] J. Ye, J. Jiang, Z. Zhou, Z. Weng, Y. Xu, L. Liu, W. Zhang, Y. Yang, J. Luo, X. Wang, *ACS Nano* **2021**, *15*, 13692.
[23] A. I. Garbe, A. Roscher, C. Schuler, A. H. Lutter, M. Glosmann, R. Bernhardt, M. Chopin, U. Hempel, L. C. Hofbauer, S. Rammelt, M. Egerbacher, R. G. Erben, R. Jessberger, *J. Bone Miner. Res.* **2012**, *27*, 2085.
[24] L. Xing, E. M. Schwarz, B. F. Boyce, *Immunol. Rev.* **2005**, *208*, 19.
[25] D. Park, J. A. Spencer, B. I. Koh, T. Kobayashi, J. Fujisaki, T. L. Clemens, C. P. Lin, H. M. Kronenberg, D. T. Scadden, *Cell Stem Cell* **2012**, *10*, 259.
[26] Z. Yuan, B. Tao, Y. He, C. Mu, G. Liu, J. Zhang, Q. Liao, P. Liu, K. Cai, *Biomaterials* **2019**, *223*, 119479.
[27] a) E. van Beek, M. Hoekstra, M. van de Ruit, C. Lowik, S. Papapoulos, *J. Bone Miner. Res.* **1994**, *9*, 1875; b) R. G. Russell, N. B. Watts, F. H. Ebetino, M. J. Rogers, *Osteoporosis Int.* **2008**, *19*, 733.
[28] A. Swami, M. R. Reagan, P. Basto, Y. Mishima, N. Kamaly, S. Glavey, S. Zhang, M. Moschetta, D. Seevaratnam, Y. Zhang, J. Liu, M. Memarzadeh, J. Wu, S. Manier, J. Shi, N. Bertrand, Z. N. Lu, K. Nagano, R. Baron, A. Sacco, A. M. Roccaro, O. C. Farokhzad, I. M. Ghobrial, *Proc. Natl. Acad. Sci. USA* **2014**, *111*, 10287.
[29] X. Zhang, B. Tan, Y. Wu, M. Zhang, J. Liao, *Polymers (Basel)* **2021**, *13*, 2100.
[30] E. de Klerk, P. A. 't Hoen, *Trends Genet.* **2015**, *31*, 128.
[31] E. Cenni, D. Granchi, S. Avnet, C. Fotia, M. Salerno, D. Micieli, M. G. Sarpietro, R. Pignatello, F. Castelli, N. Baldini, *Biomaterials* **2008**, *29*, 1400.

ADVANCED FUNCTIONAL MATERIALS

Supporting Information

for *Adv. Funct. Mater.,* DOI: 10.1002/adfm.202214126

Multifunctional BPs/MT@PLGA-ALE Nanospheres for Treatment of Osteoporotic Fracture with Near-Infrared Irradiation

Kai Zheng, Jiaxiang Bai, Wanling Chen, Yaozeng Xu, Huilin Yang, Wei Li, Penghui Li, Liping Tong,* Huaiyu Wang,* Paul K. Chu, and Dechun Geng**

WILEY-VCH

Supporting Information

Multifunctional BPs/MT@PLGA-ALE nanospheres for treatment of osteoporotic fracture with near-infrared irradiation

Kai Zheng[#], Jiaxiang Bai[#], Wanling Chen[#], Yaozeng Xu, Huilin Yang, Wei Li, Penghui Li, Liping Tong*, Huaiyu Wang*, Paul K. Chu, Dechun Geng**

K. Zheng, J. Bai, Prof. Y. Xu, Prof. H. Yang, Prof. D. Geng

Department of Orthopedics, The First Affiliated Hospital of Soochow University, 188 Shizi Road, Suzhou 215006, Jiangsu, China

E-mail: szgengdc@suda.edu.cn (D. Geng)

W. Chen, Dr. W. Li, Dr. P. Li, Prof. L. Tong, Prof. H. Wang

Center for Human Tissues and Organs Degeneration, Shenzhen Institute of Advanced Technology, Chinese Academy of Sciences, Shenzhen 518055, China

E-mail: ph.li@siat.ac.cn; (P. Li); lp.tong@siat.ac.cn; (L. Tong); hy.wang1@siat.ac.cn (H. Wang)

Prof. Paul K. Chu

Department of Physics, Department of Materials Science and Engineering, and Department of Biomedical Engineering, City University of Hong Kong, Tat Chee Avenue, Hong Kong, China

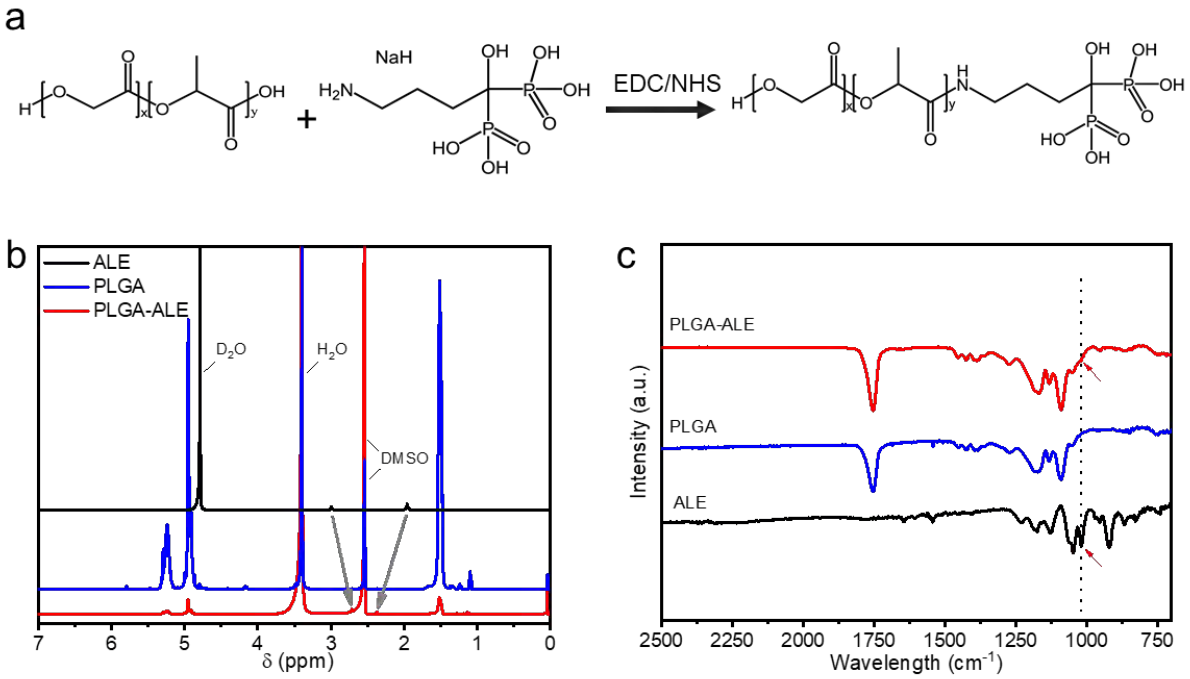

Figure S1. (a) Schematic illustration of functionalization of PLGA with the ALE ligand; (b, c) ^{1}H NMR spectra and FT-IR spectra of ALE, PLGA and PLGA-ALE.

Table S1. Concentration of the BP/MT@PLGA-ALE NSs and loading efficiency of BPs and MT.

	Concentration (mg/mL)	BPs loading (%)	MT loading (%)
BPs/MT@PLGA-ALE NSs	1.04±0.04	5.91±0.17	2.73±0.15

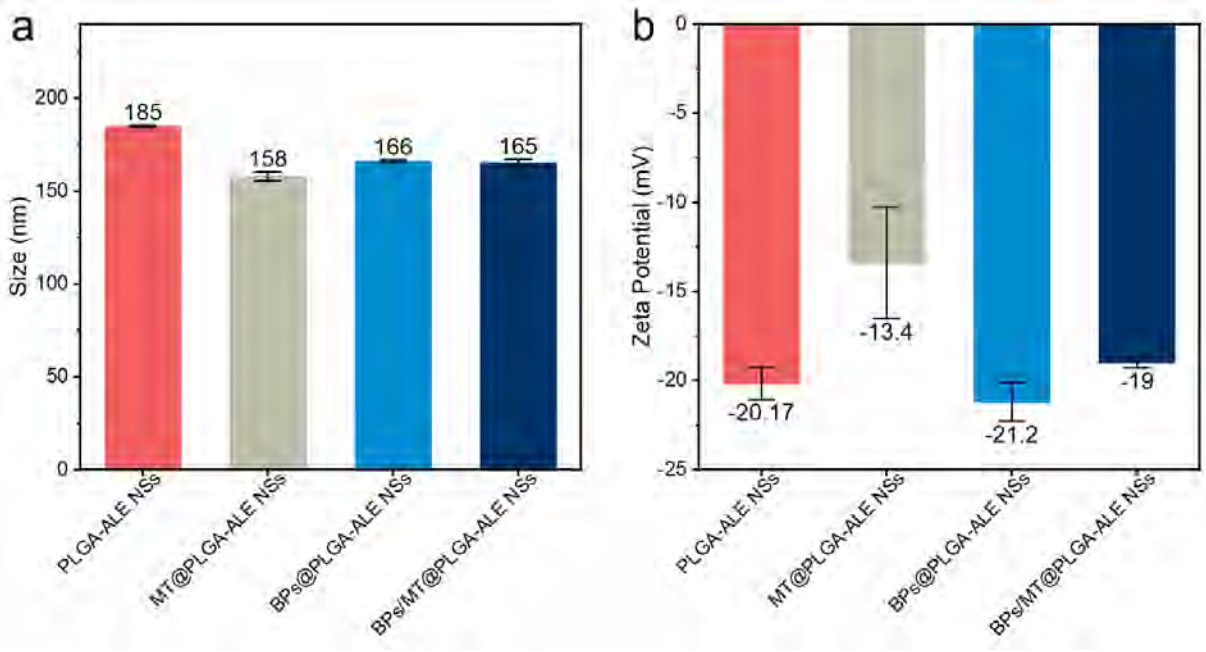

Figure S2. (a) Size and (b) Zeta potentials of PLGA-ALE NSs, MT@PLGA-ALE NSs, BPs@PLGA-ALE NSs and BPs/MT@PLGA-ALE NSs.

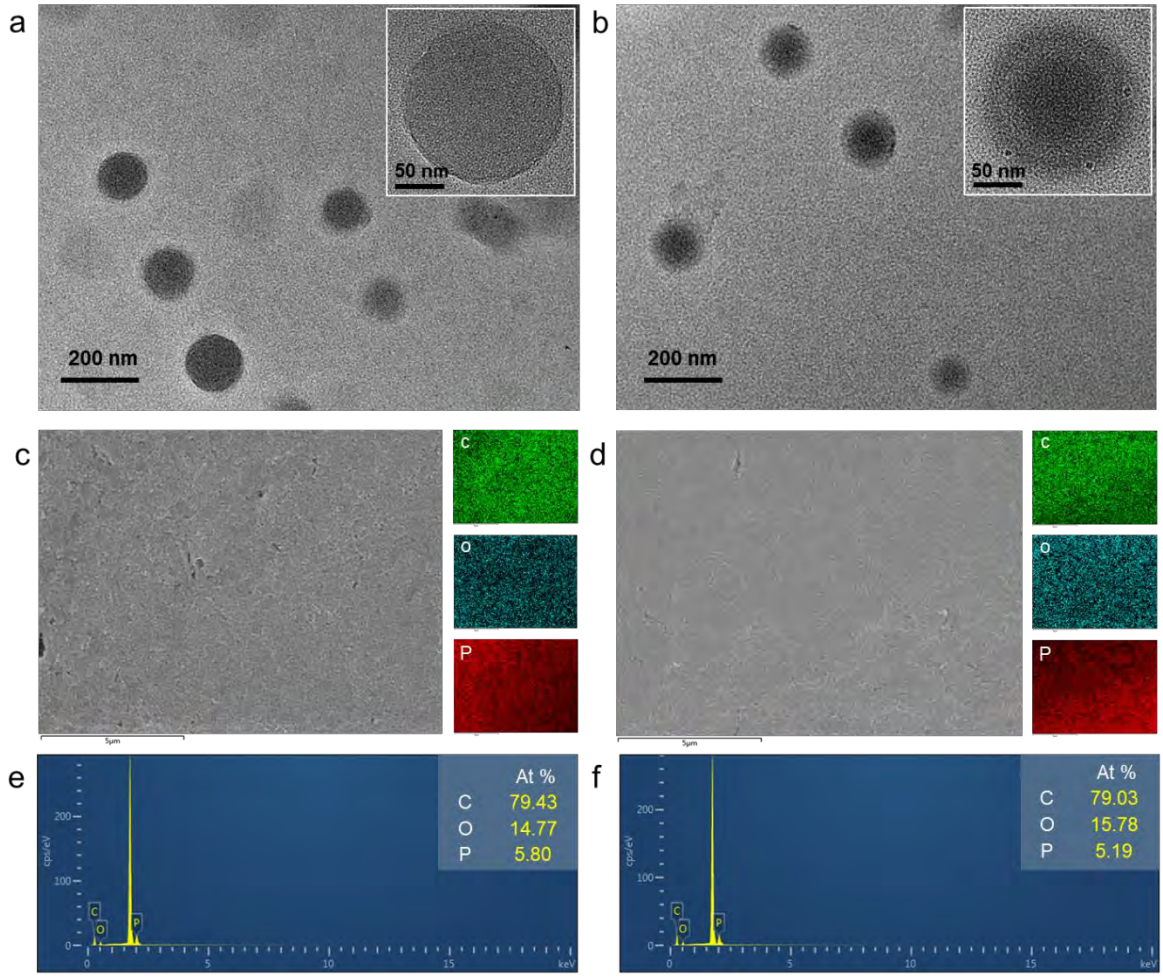

Figure S3. (a, b) TEM images of PLGA-ALE NSs and BPs/MT@PLGA-ALE NSs; Images and elemental maps by EDS: (c, e) BPs@PLGA-ALE NSs and (d, f) BPs/MT@PLGA-ALE NSs.

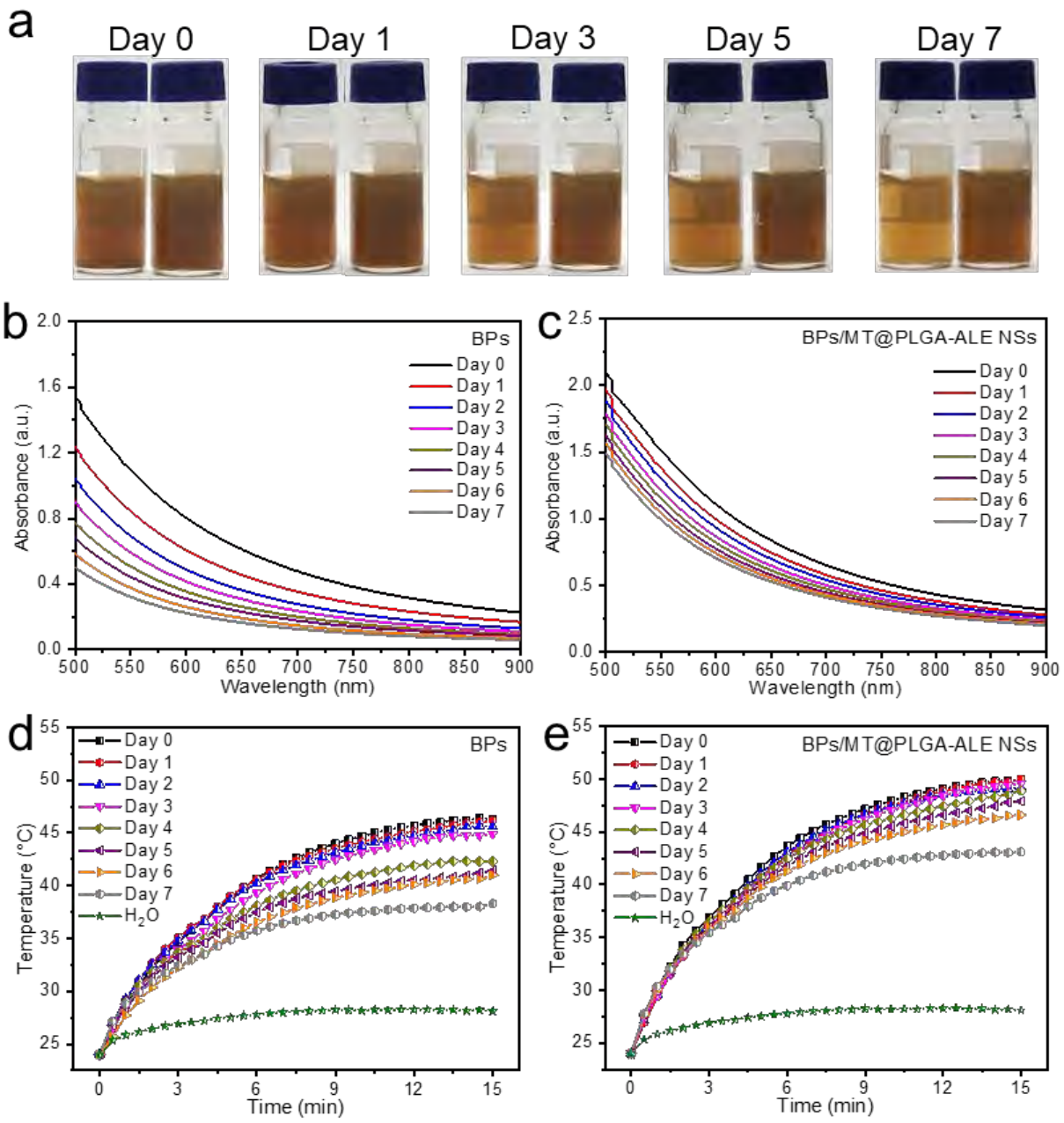

Figure S4. (a) Photographs of BPs (left) and BPs/MT@PLGA-ALE NSs (right) dispersed in water at room temperature for different time; (b, c) Absorption spectra of BPs and BPs/MT@PLGA-ALE NSs dispersed in water at room temperature for different time; (d, e) Photothermal heating curves of BPs and BPs/MT@PLGA-ALE NSs dispersed in water at room temperature for different of time and then irradiated with the 808 nm laser.

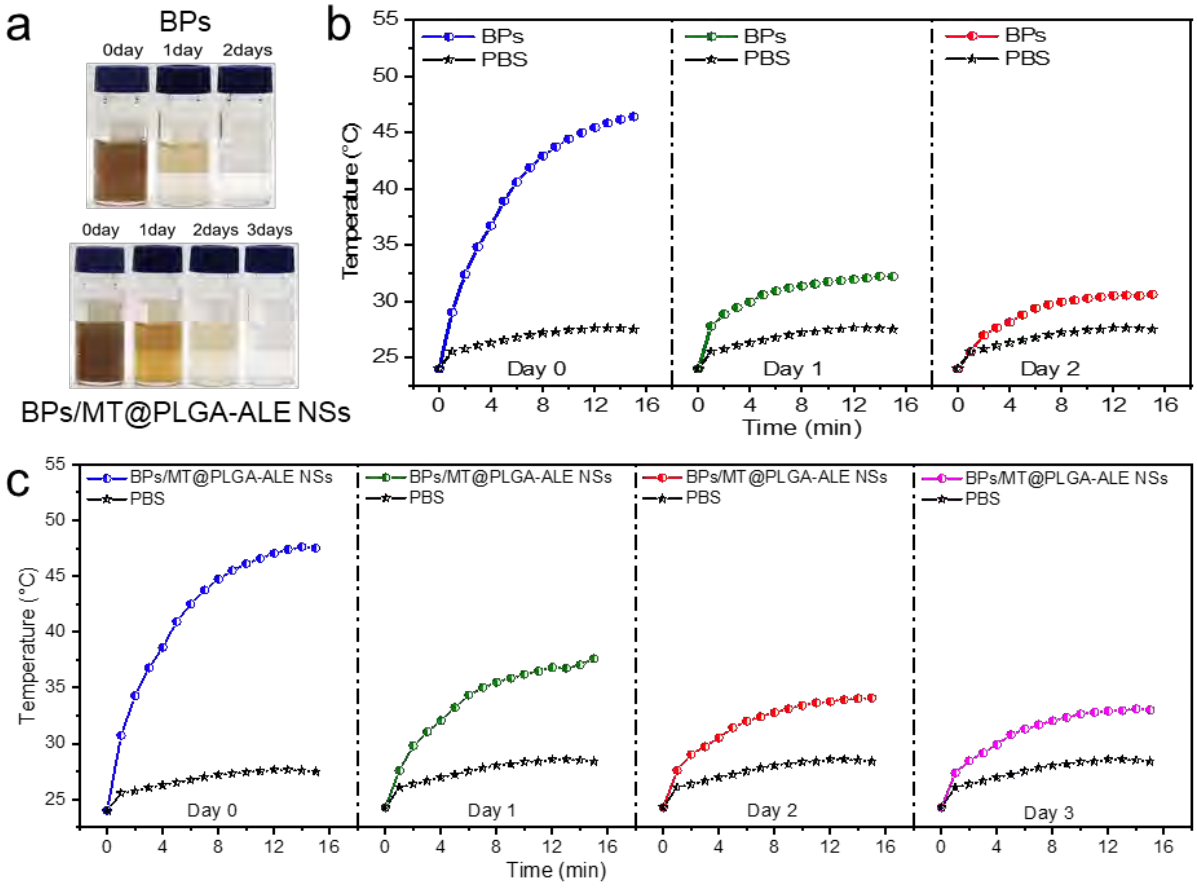

Figure S5. (a) Photographs of BPs and BPs/MT@PLGA-ALE NSs dispersed in PBS at 37 °C for different time; (b, c) Photothermal heating curves of BPs and BPs/MT@PLGA-ALE NSs dispersed in PBS at 37 °C for different time and then irradiated with the 808 nm laser.

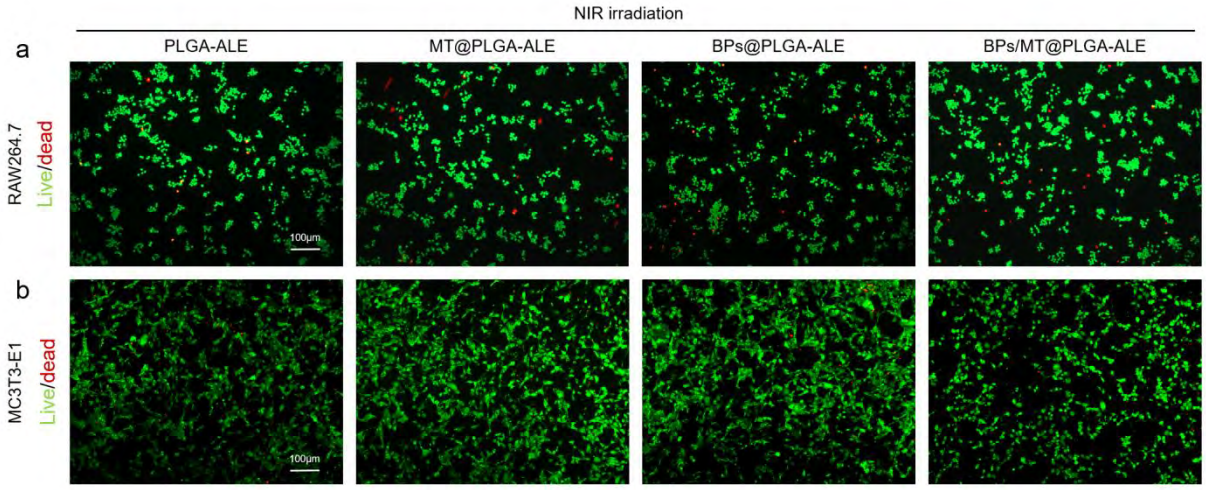

Figure S6. (a, b) Live/dead staining of the RAW264.7 and MC3T3-E1 cells incubated with PLGA-ALE NSs, MT/PLGA-ALE NSs, BPs/PLGA-ALE NSs and BPs/MT/PLGA-ALE NSs at a concentration of 12.5 μg/mL for 72 hours prior to 808 nm NIR illumination.

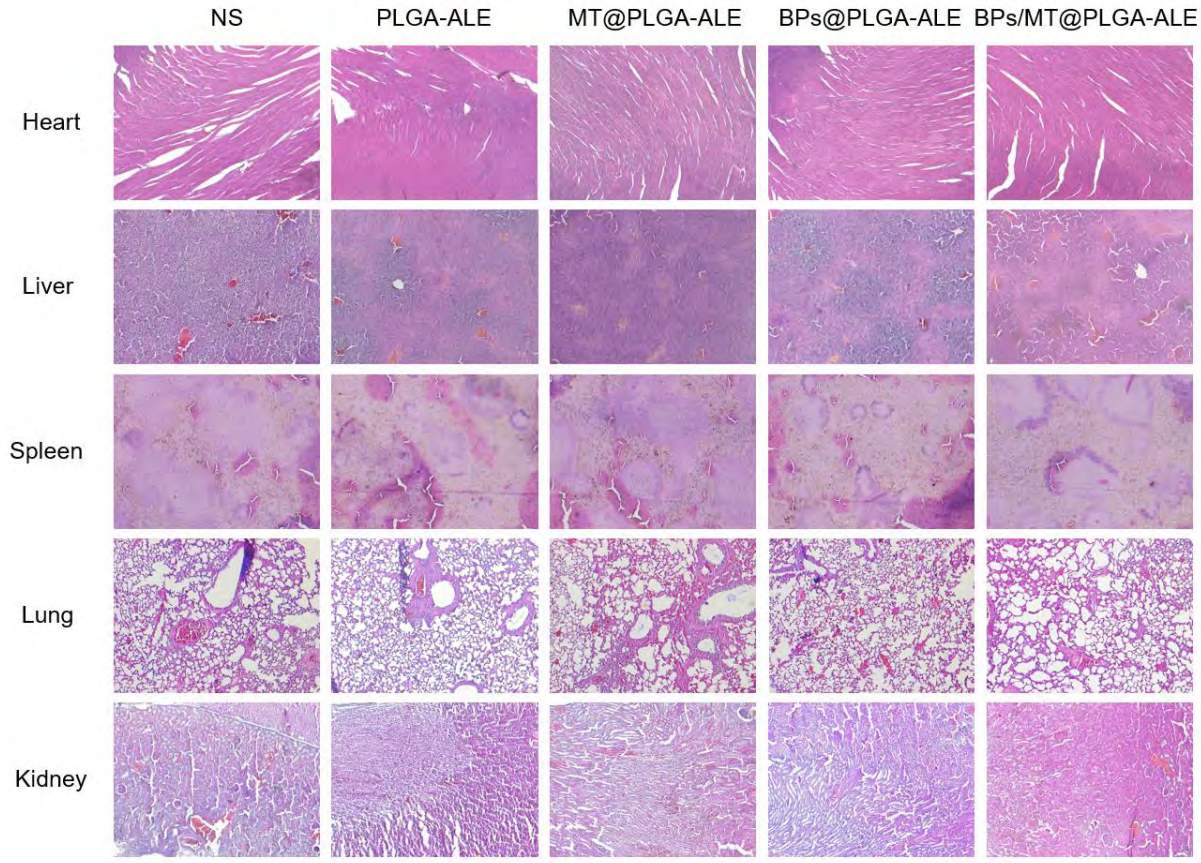

Figure S7. H&E stained sections of the heart, liver, spleen, lung and kidney in mice after 3 months of weekly different treatments.

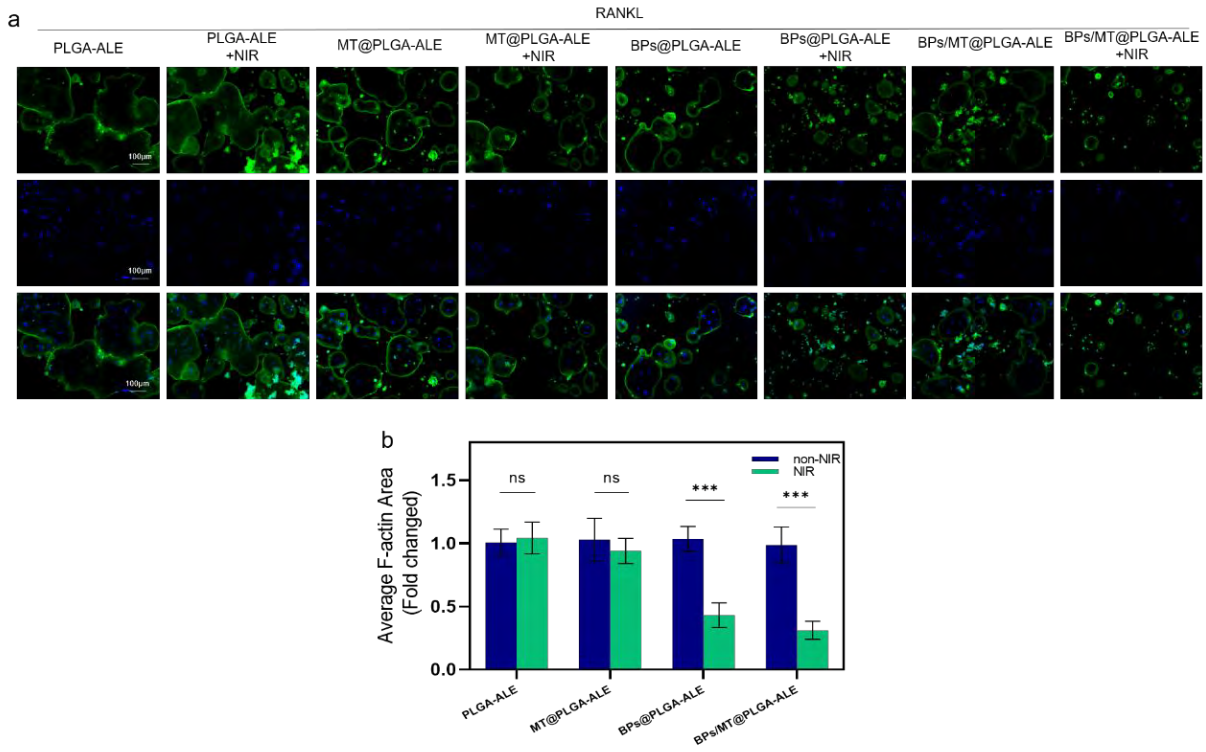

Figure S8. (a) F-actin staining of the RANKL-induced RAW264.7 cells treated with the PLGA-ALE NSs, MT@PLGA-ALE NSs, BPs@PLGA-ALE NSs and BPs/MT@PLGA-ALE NSs with or without NIR irradiation; (b) Quantitative evaluation of the F-actin areas (n=3 per group, *** denotes $p < 0.001$).

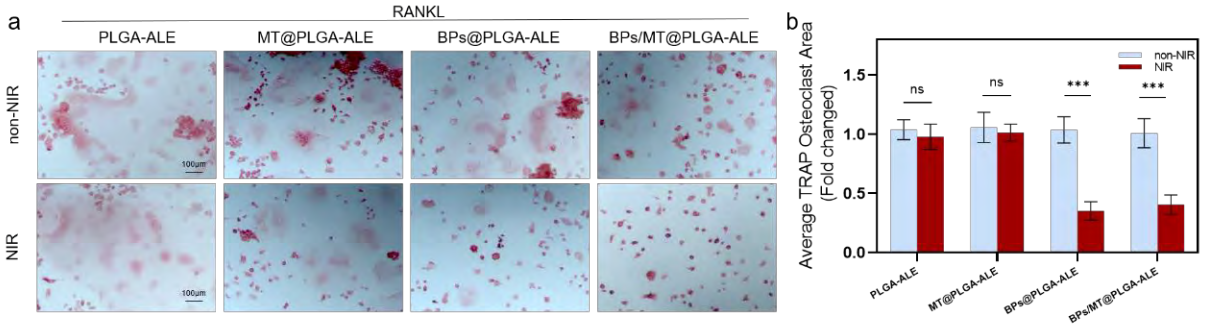

Figure S9. (a) TRAP staining of the RANKL-induced RAW264.7 cells treated with the PLGA-ALE NSs, MT@PLGA-ALE NSs, BPs@PLGA-ALE NSs and BPs/MT@PLGA-ALE NSs with or without NIR irradiation; (b) Quantitative evaluation of the TRAP-positive areas (n=3 per group, *** denotes $p < 0.001$).

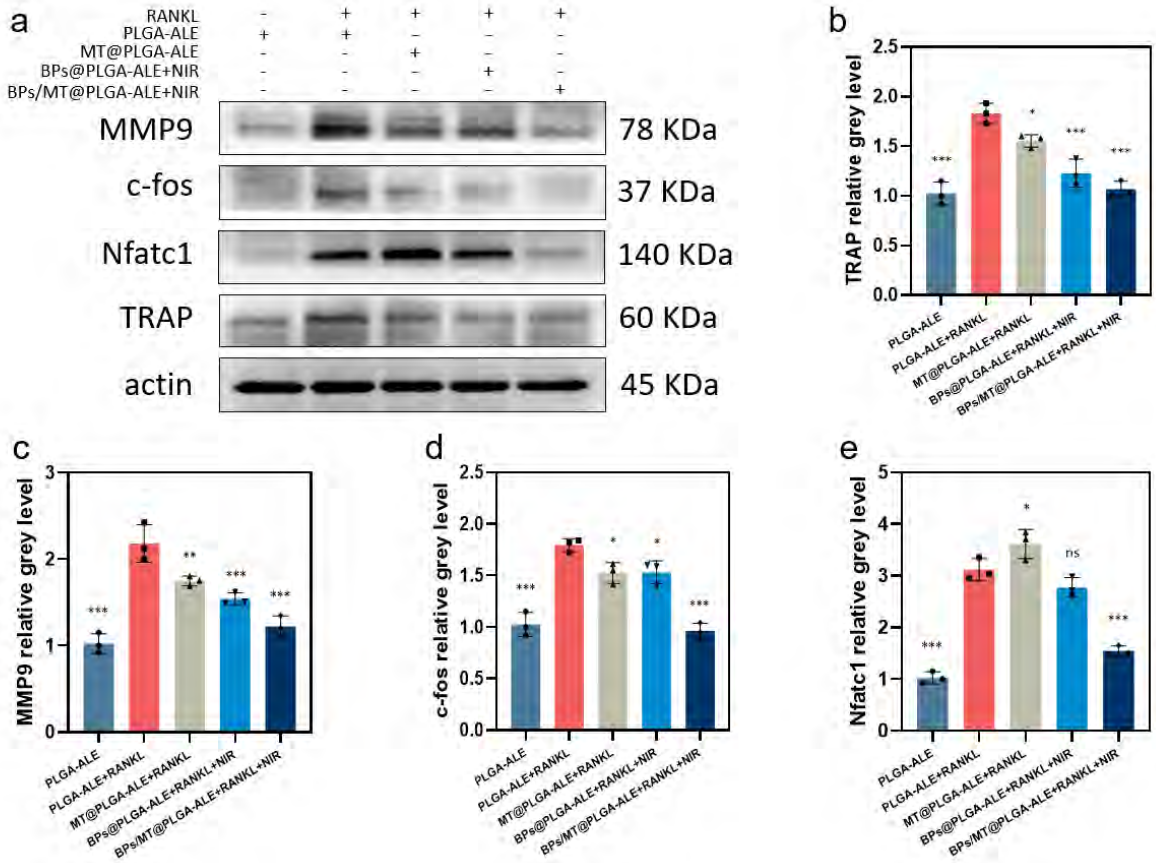

Figure S10. (a) Western blot analysis of the MMP9, c-fos, Nfatc1 and TRAP in RAW264.7 cells after different treatments; (b-e) Semiquantitative analysis of the protein levels (n=3 per group, * denotes $p < 0.05$, ** denotes $p < 0.01$, and *** denotes $p < 0.001$ compared to the PLGA-ALE + RANKL group).

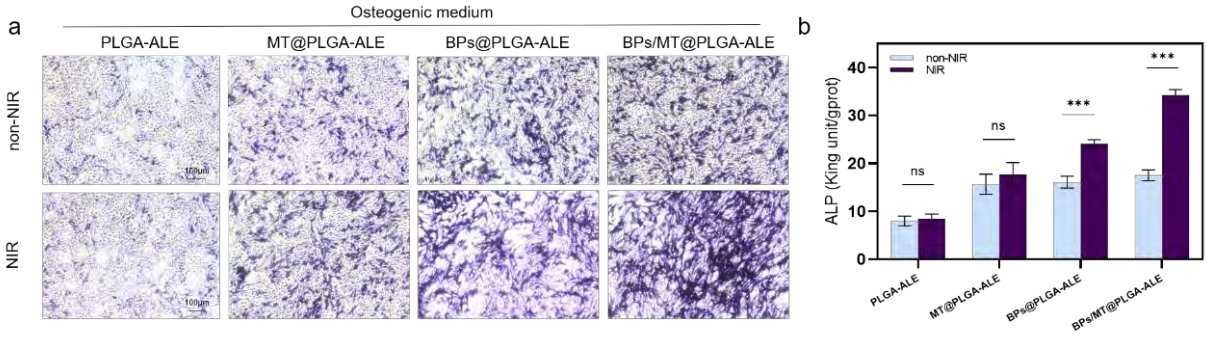

Figure S11. (a) ALP staining of the MC3T3-E1 cells incubated with the PLGA-ALE NSs, MT@PLGA-ALE NSs, BPs@PLGA-ALE NSs and BPs/MT@PLGA-ALE NSs with or without NIR irradiation; (b) Quantitative evaluation of ALP activities (n=3 per group, *** denotes $p < 0.001$).

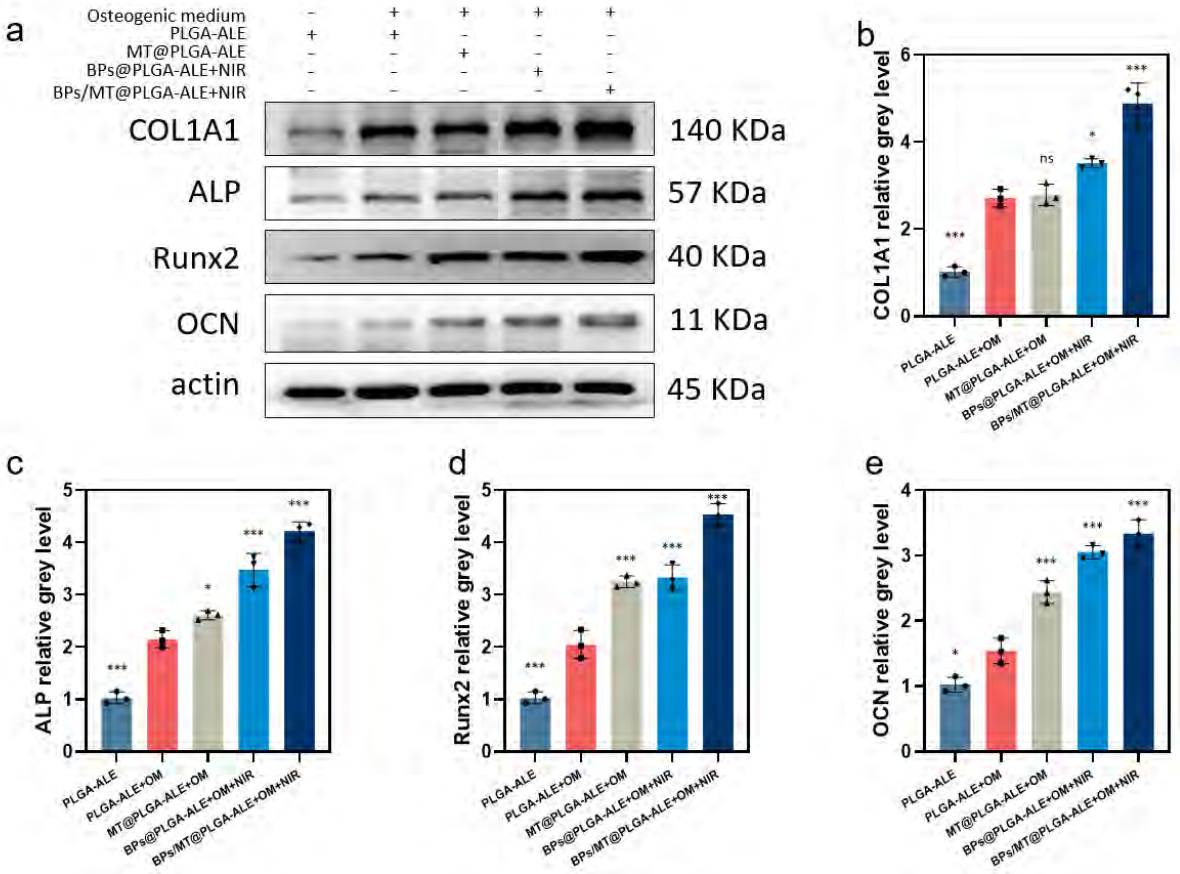

Figure S12. (a) Western blotting of the COL1A1, ALP, Runx2 and OCN in MC3T3-E1 cells after different treatments; (b-e) Semiquantitative analysis of the protein levels (n=3 per group, * denotes $p < 0.05$ and *** denotes $p < 0.001$ compared to the PLGA-ALE + Osteogenic induction group).

Table S2. Primer sequences used in real-time PCR.

Gene	Forward Primers (5'-3')	Reverse Primers (5'-3')
GAPDH	GGTTGTCTCCTGCGACTTCA	TGGTCCAGGGTTTCTTACTCC
MMP9	CTGGACAGCCAGACACTAAAG	CTCGCGGCAAGTCTTCAGAG
TRAP	TGTGGCCATCTTTATGCT	TTCGGGGTTTCTTTACTG
Nfatc1	GAGAATCGAGATCACCTCCTAC	TTGCAGCTAGGAAGTACGTCTT
atp6v0d2	GTGAGACCTTGGAAGACCTGAA	TCGGGGACTCGTGTAAAGAG
COL1A1	GCTCCTCTTAGGGGCCACT	CCACGTCTCACCATTGGGG
Runx2	CCTTCAAGGTTGTAGCCCTC	GGAGTAGTTCTCATCATTCCCG
OCN	TTGAACTGTTTGTTTTGGACCC	CCAACAGACACCAGTTGTAAAG
ALP	CAGCGGGTAGGAAGCAGTTTC	CCCTGCACCTCATCCCTGA
Bcl2	GAGACAGCCAGGAGAAATCA	CCTGTGGATGACTGAGTACC
Fas	TATCAAGGAGGCCCATTTTGC	TGTTTCCACTTCTAAACCATGCT
Caspase 7	AAGACGGAGTTGACGCCAAG	CCGCAGAGGCATTTCTCTTC
Nlrc4	ATCGTCATCACCGTGTGGAG	GCCAGACTCGCCTTCAATCA
Caspase 1	GCTCTGCGGTGTAGAAAAG	ATAGGTCCCGTGCCTTG
Il-18	GGAGGGTTTGTGTTCCAG	AATACAGGCGAGGTCATCA

Abbreviations: GAPDH: glyceraldehyde 3-phosphate dehydrogenase; MMP9: matrix metalloprotein 9; TRAP: Tartrate-resistant acid phosphatase; NFatc1: nuclear factor of activated T-cells, cytoplasmic, calcineurin-dependent 1; Atp6v0d2: ATPase H^+ Transporting V0 Subunit D2; COL1A1: collagen type I alpha 1; Runx2: Runt-related transcription factor 2; OCN: Osteocalcin; ALP: Alkaline phosphatase; Bcl2: B-cell lymphoma-2; Fas: TNF receptor superfamily member 6; Caspase 7: cysteinyl aspartate specific proteinase 7; Nlrc4: NLR family, CARD domain containing 4; Caspase 1: cysteinyl aspartate specific proteinase 1; Il-18: interleukin-18.

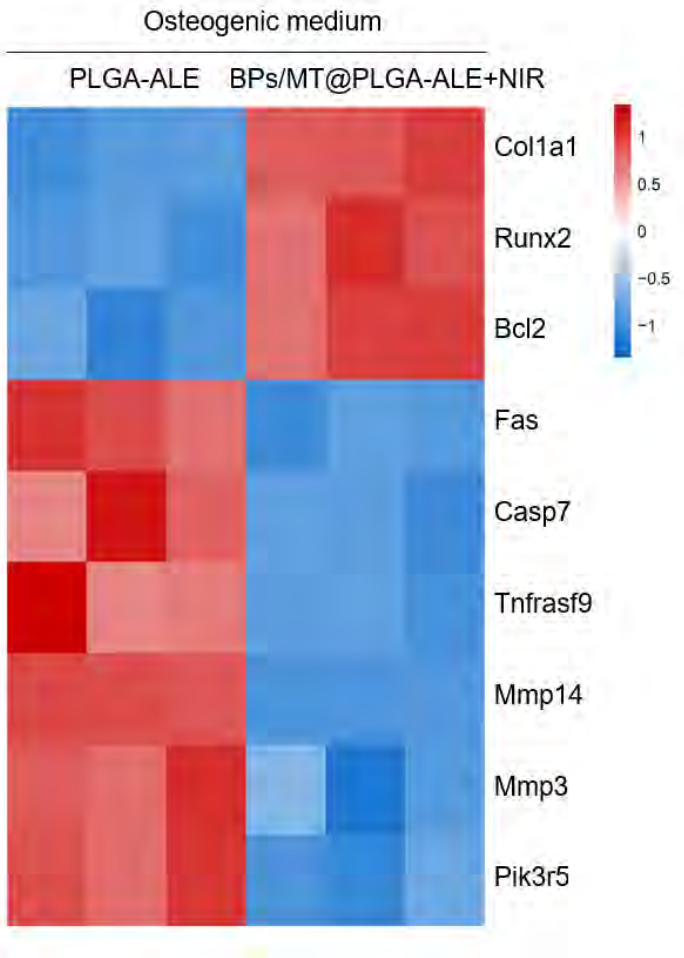

Figure S13. Differential expression of the osteoblast-related biomarkers in TNF and apoptosis signaling pathways in the osteogenic-induced MC3T3-E1 cells of the PLGA-ALE and BPs/MT@PLGA-ALE+NIR groups.

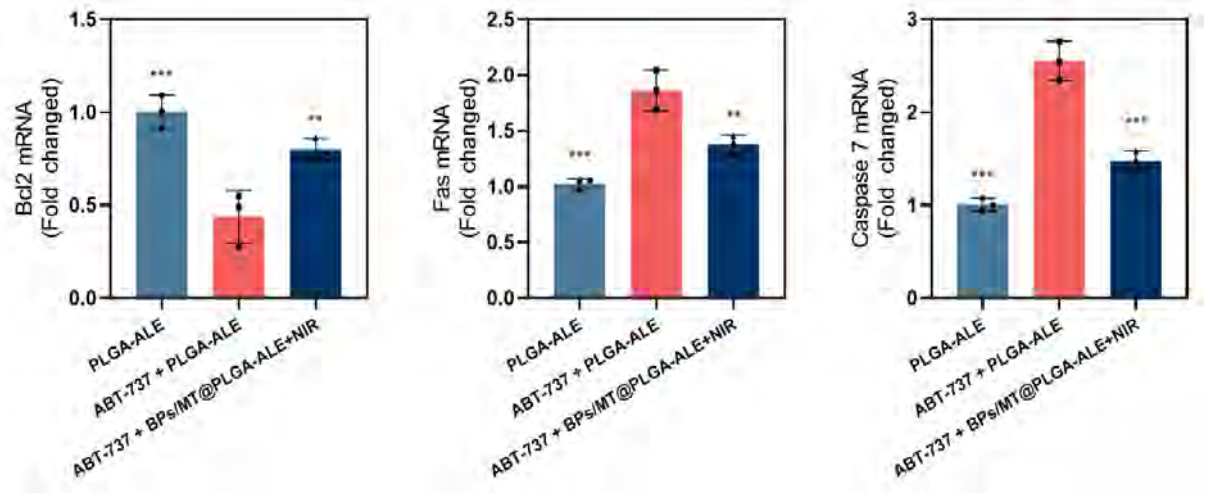

Figure S14. Gene levels of Bcl2, Fas and Caspase 7 (n=3 per group, ** denotes $p < 0.01$, and *** denotes $p < 0.001$ compared to the ABT-737 + PLGA-ALE group).

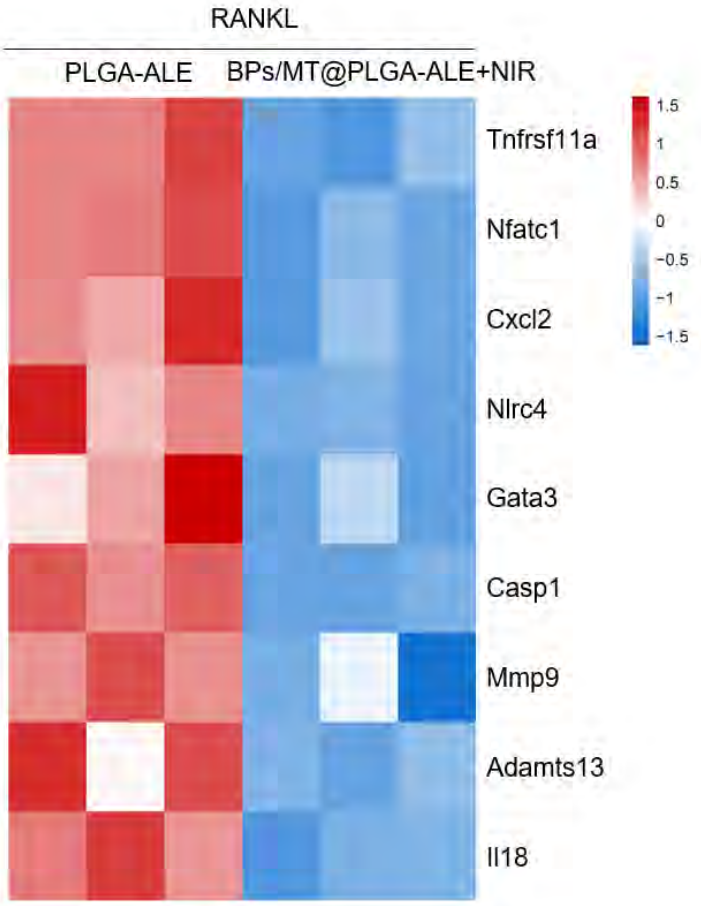

Figure S15. Differential expression of the osteoclast-related biomarkers in TNF and NOD-like receptor signaling pathways in RANKL-induced RAW264.7 cells of the PLGA-ALE and BPs/MT@PLGA-ALE+NIR groups.

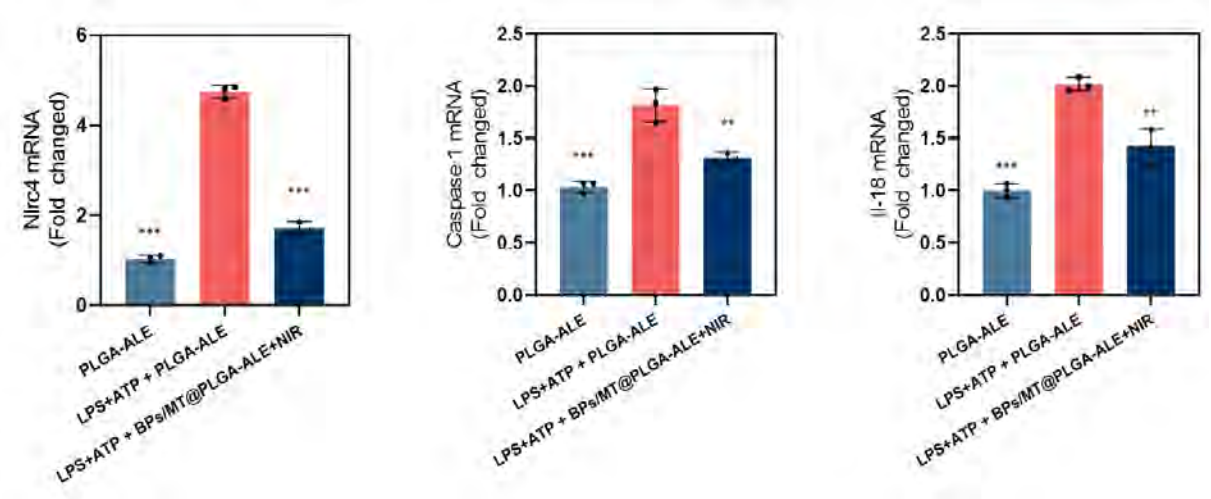

Figure S16. Gene levels of Nlrc4, Caspase 1 and Il-18 (n=3 per group, ** denotes $p < 0.01$, and *** denotes $p < 0.001$ compared to the LPS+ATP + PLGA-ALE group).